Novel algorithms for efficiently accumulating, analysing and visualising full-waveform LiDAR in a volumetric representation with applications to forestry

submitted by

Milto Miltiadou

for the degree of Doctor of Engineering

of the

University of Bath

Centre for Digital Entertainment

and of the

Plymouth Marine Laboratory

NERC Airborne Research Facility

April 2017

COPYRIGHT

Signature of Author.....

Milto Miltiadou

Abstract

no more than 300 words

NOTES:

Blue colour: additions according to Neill's feedback,

Purple colour: addition/corrections according to Mike's comments

Red colour: notes

Gray colour: text that is going to be modified

To be added on top

Abstract

This study focuses on enhancing the visualisations and classifications of forested areas using coincident full-waveform (fw) LiDAR data and hyperspectral images. The ultimate aim is use both datasets to derive information about forests and show the results on a 3D virtual, interactive environment. Influenced by Persson et al (2005), voxelisation is an integral part of this research. The intensity profile of each full-waveform pulse is accumulated into a voxel array, building up a 3D density volume. The correlation between multiple pulses into a voxel representation produces a more accurate representation, which confers greater noise resistance and it further opens up possibilities of vertical interpretation of the data. The 3D density volume is then aligned with the hyperspectral images using a 2D grid similar to Warren et al (2014) and both datasets are used in visualisations and classifications.

Previous work in visualising fw LiDAR has used transparent objects and point clouds, while the output of this system is a coloured 3D-polygon representation, showing well-separated structures such as individual trees and greenhouses. The 3D density volume, generated from the fw LiDAR data, is polygonised using functional representation of object (FReps) and the marching cubes algorithm (Pasko and Savchenko, 1994) (Lorensen and Cline, 1987). Further, an optimisation algorithm is introduced that uses integral volumes (Crow, 1984) to speed up the process of polygonising the volume. This optimisation approach not only works on non-manifold object, but also a speed up of up to `51%` was achieved. The polygon representation is also textured by projecting the hyperspectral images into the mesh. In addition, the output is suitable for direct rendering with commodity 3D-accelerated hardware, allowing smooth visualisation.

In future work, the effects of combining both hyperspectral imagery and fw LiDAR in classifications and visualisations are examined. At first, two pixel wise classifiers, a support vector machine and a Bayesian probabilistic model, will be used for testing the effects of the combination in generating tree coverage maps. Higher accuracy classification results are expected when metrics from both datasets are used together. Regarding the visualisations, the differences of applying surface reconstruction versus direct volumetric rendering will be discussed and an ordered tree structure with integral sums of the node values will be used for speeding up the ray-tracing of direct volumetric rendering and improving memory management of aforementioned optimisation algorithm with integral volumes. Further, deferred rendering is suggested for testing the visual human perception of projecting multiple bands of the hyperspectral images on the FW LiDAR

polygon representations. At the end of this project the combination of the datasets will be used along with the watershed algorithm for tree segmentation, which is useful for measuring the stem density of a forest and for tree species classifications.

from EDE:

Firstly, a new and fast way of aligning the FW LiDAR with Remotely Sensed Images has been developed in DASOS and by generating tree coverage maps it was shown that the combination of those datasets confers better remote survey results. This work was presented at the 36th ISRSE International Conference.

Secondly, automated detection of dead trees in native Australian forests has a significant role in protecting animals, which live in those trees and are close to extinction. DASOS allow the generation of 3D signatures characterising dead trees. A comparison between the discrete and FW LiDAR is performed to demonstrate the increased survey accuracy obtained when the FW LiDAR are used.

Finally, the last application is for improving visualisations for foresters. Foresters have a great knowledge about forests and can derive a wealth of information directly from visualisations of the remotely sensed data. This reduces the travelling time and cost of getting into the forests. This research optimises visualisations by using the new FW LiDAR representations and a speed of up to 51% has been achieved.

FW LiDAR has great potentials in forestry and this research has already started to have an impact in the FW LiDAR community by making those huge datasets easier to handle. DASOS is now used at Interpine Group Ltd, a world leading Forestry Company in New Zealand and it has been tested from a PhD student at Bournemouth University who looks into estimating bird distribution in the New Forest. In the future, it is expected that DASOS will be widely used in remote forest surveys (i.e. estimating the commercial value of a forest and detecting infected trees at early stages for treatment).

Acknowledgements

Above all, I would like to express my great gratitude to my industrial supervisors Dr. Michael Grant who had supported me continuously during my research and gave me the freedom to create a project of my own interest.

Then, I would like to thanks Dr. Matthew Brown, who helped me during my first years of my studies by giving me valuable and informative feedback. He was always there to keep me working on the right track.

Equally important is my current supervisor Dr. Neil D.F. Campbell and he is not to be missed from the acknowledgements.

Furthermore, special thanks are given to Dr. Mark Warren, Dr. Darren Cosker, MSc Susana Gonzalez Aracil and Dr. Ross Hill who occasionally advised me during my studies.

It further worth giving credits to my data providers, the Natural Environment Research Council's Airborne Research Facility (NERC ARF) and Interpine Group Ltd.

Last but not least, I am extremely grateful to my funding organisations, the Centre for Digital Entertainement and Plymouth Marine Laboratory, who supported financially and consequently made this research possible.

Abbreviations and Glossary

AGC	Automatic Gain Controller
ALS	Airborne Laser Scanning
APL	Airborne Processing Library
ARF	Airborne Research Facility
CG	Computer Graphics
CHM	Canopy Height Model
CUDA	parallel computing platform available on nvidia graphic cards
DASOS	($\delta\alpha\sigma\sigma\varsigma$=forest in Greek), the open source software implemented for managing FW LiDAR data
DBH	Diameter at Breast Height
DEM	Digital Elevation Model
DTM	Digital Terrain Model (DTM)
FW	Full-Waveform
GB	Gigabyte
GPU	Graphics Processing Unit
LiDAR	Light Detection And Ranging
MRI	Magnetic Resonance Imaging
NASA	National Aeronautics and Space Administration
NDVI	Normalised Difference Vegetation Index
NERC	Natural Environment Research Council
NIR	Near-Infrared Region of the electromagnetic spectrum
QGIS	Quantum Geographic Information System
SIMD	Single Instruction, Multiple Data
TB	Terabyte
VIS	VIsual Spectrum
VLR	Variable Length Records
WPDF	Waveform Packet Descriptor Format
UK	United Kingdom

Publications

DASOS-User Guide, M. Miltiadou, N.D.F Campbell, M. Brown, S.C. Aracil, M.A. Warren, D. Clewley, D.Cosker, and M. Grant, Full-waveform LiDAR workshop at Interpine Group Ltd, Rotorua NZ, 2016

Improving and Optimising Visualisations of full-waveform LiDAR data, M. Miltiadou, M. Brown, N.D.F Campbell, D. Cosker, M. Grant, *EuroGraphics UK, Computer Graphics & Visual Computing*, 2016

University of Bath **Alignment of Hyperspectral Imagery and Full-Waveform LiDAR data for visualisation and classification purposes**, M. Miltiadou, M. A. Warren, M. Grant, and M. Brown, *The International Archives of Photogrammetry, Remote Sensing and Spatial Information Sciences*, vol. 40, no. 7, p. 1257, 2015.

Reconstruction of a 3D Polygon Representation from Full-Wavefrom LiDAR data, M. Miltiadou, M. Grant, M. Brown, M. Warren, and E. Carolan,*RSPSoc Annual Conference, New Sensors for a Changing World*, 2014.

Awards

EDE and Ravenscroft Prize - Finalist: Selected as one of the five finalists for this is a prestigious prize that recognises the work of best postgraduate researchers.

Student Poster Competition at Silvilaser.

Conference Presentations

Remote Sensing Cyprus (RSCy) Conference, 2017 , Paphos, Cyprus - Oral Presentation

ForestSAT Conference,2016 , Santiago, Chile - Oral Presentation

Computer Graphics & Visual Computing (CGVC),2016, Bournemouth, United Kingdom - Poster Presentation

Silvilaser, 2015, La Grant Motte, France - Oral Presentation

International Symposium of Remote Sensing of the Environment (ISRSE), 2015, Berlin, German - Oral Presentation

Remote Sensing and Photogrammetry Society (RSPSoc) Conference, New Sensors for a Changing world , 2014, Aberystwyth, United Kingdom - Oral Presentation

Workshops

Full day workshop about FW LiDAR and DASOS at *Interpine Ltd Group*, 2016, Rotorua, New Zealand

Demonstration of DASOS_v2 at the practical LiDAR session at *the NERC ARF annual workshop*, 2017, Plymouth, United Kingdom

Contents

List of Figures

Chapter 1

Introduction

1.1 Forest Monitoring: Importance and Applications

1.2 Background Information about Remote Sensing and Airborne Laser Scanning Systems

Remote sensing refers to the acquisition of information about objects, for example vegetation and archaeological monuments, without physical contact and the subsequent interpretation of that information. The sensors used to capture the information are divided into passive and active. For example satellite photography is passive because information are collected from the reflected natural sun light, while Airborne Laser Scanners (ALS) are active because they emit laser beams and collects information from the backscattered laser energy [1].

According to Wanger et al, Airborne Laser Scanning (ALS) is a growing technology used in environmental research to collect information about the Earth, such as vegetation and tree species. Comparing ALS with traditional photography, ALS is not influenced by light and it is therefore less dependent on weather conditions (ie. it collects information from below the clouds, or at night). The laser beam also partially penetrates the tree canopies allowing it to record information about the forest structure below the canopy, as well as the ground [2]. ALS methods are divided into pulse systems, which repeatedly emit pulses, and continuous wavelength systems that continuously emit light. They both acquire information from the backscattered laser intensity over time, but continuous wavelength systems are more complicated because they obtain one extra physical parameter, the frequency of the ranging signal. Further, according to Wehr and Lohr, continuous wavelength systems are 85 times less accurate than pulse systems [3].

LiDAR (Light Detection And Ranging) systems are active and pulse laser scanning systems [3]. They are divided into two groups according to the diameter of the footprint left by the laser beam on the ground, which is primarily dependent on the distance between the sensor and the target (altitude, in most remote sensing) and the beam divergence. The small-footprint group has a 0.2-3m diameter, is widely commercialised and the sensors are mostly carried on planes (ALS systems). In contrast, the large-footprint systems have a wider diameter (10-70m) and during experiments they were mostly mounted on satellites. Small-footprint systems record at higher resolution but cannot guarantee that every pulse will reach the ground due to the small diameter of their footprint, making topographic measurements difficult, and are limited to smaller survey areas due to the cost and availability of aircraft. In contrast, large-footprint scanners have wider diameters and can therefore scan wider areas with the likelihood of recording the ground to be higher [4] .

In addition, there are two types of LiDAR data: discrete and full-waveform (FW). Discrete LiDAR records a few peaks of the reflected laser intensity, while FW LiDAR stores the entire backscattered signal. The discrete LiDAR has been widely used and a 40% reduction of fieldwork has been achieved at Interpine Ltd Group, New Zealand, with that technology. Regarding the newer FW LiDAR, scientists understand their concepts and potentials but due to the shortage of available tools able to handle these large datasets, there are very few uses of FW LiDAR [5].

The design of the first FW LiDAR system was introduced in 1980s, but the first operational system was developed by NASA in 1999 [6]. The vastly increased amount of information recorded within the FW LiDAR suggests many new possibilities and problems from the point of view of image understanding, remote surveying and visualisation. As an indication, a 9.3GB discrete LiDAR from New Forest, UK, corresponds to 55.7GB of FW LiDAR.

This research is focused on the representation and efficient use of FW LiDAR data and contributes both to forestry visualisations and classifications. Two datasets are used for testing and evaluation: the New Forest and the RedGum dataset. An in-depth explanation of LiDAR systems and the specifications, differences and challenges of the two datasets are given in Section 2. An overview of the specific aims, objectives and contributions of this thesis, set in the context of these datasets, is then given at Section 3.

Chapter 2

Acquire Data

The aim of this section is to give a practical and scientific insight into the acquisition of data, because a good knowledge of these methods and their limitations is essential for understanding the related research undertaken. The relations between the two main datasets used in this project are depicted on Figure 2-1 and briefly explained here:

- The **New Forest dataset** from the UK was provided by the Natural Environment Research Council's Airborne Research Facility (NERC ARF). Measurements were collected simultaneously a Leica ALS50-II LIDAR and AISA Eagle/Hawk hyperspectral radiometers on the 8th of April in 2010. It contains Discrete LiDAR, FW LiDAR and hyperspectral images.

- The **RedGum dataset** was acquired in Australia using a Trimble AX60 integrated LIDAR/Camera instrument over the time period from the 6th of March in 2015 until the 31st of March in 2015. It was provided by the RPS Australia East Pty Ltd. Only the FW LiDAR data are used here.

The ALS data are explained first, because they are the main focus of this research, and hyperspectral imagery is towards the end of the chapter. In Section 2.1, an in-depth description of ALS systems and the differences between discrete and FW LiDAR data is given. Section 2.2 briefly discusses the binary file format of the acquired LiDAR data and Section 2.3 is a discussion on the limitations, the differences and the advantages of two LiDAR instruments; the Leica and Trimble. The essential information about the hyperspectral imagery, which is only associated with the New Forest dataset, is then covered in Section 2.4.

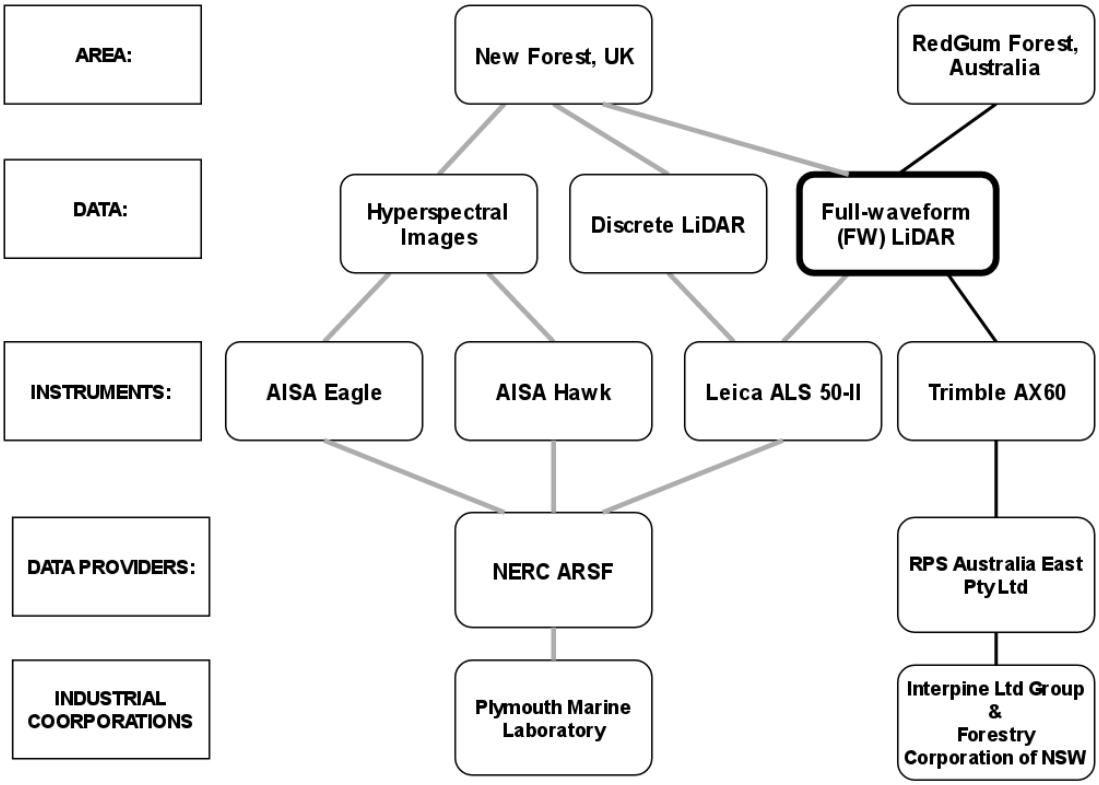

Figure 2-1: Data and Instruments

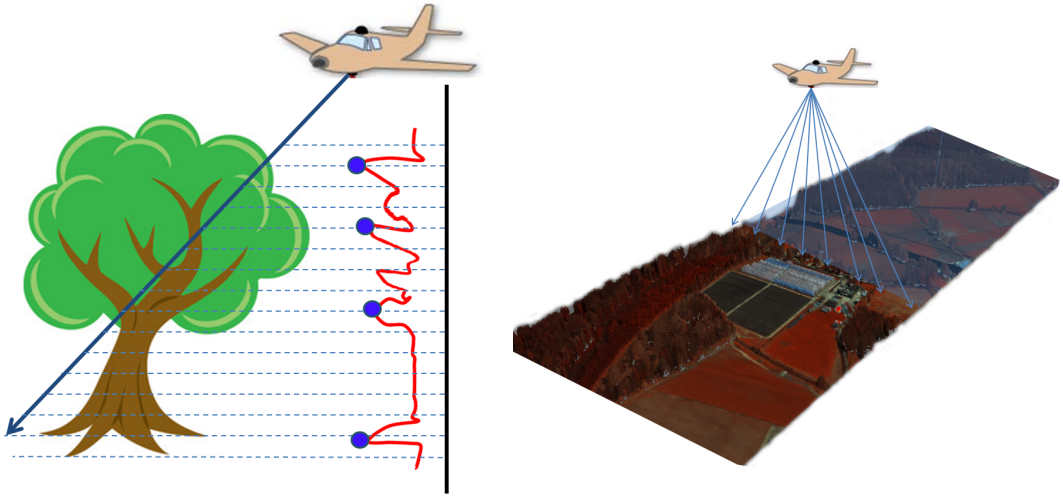

(a) A Pulse: Discrete Vs Full-Waveform (b) A Flightline

Figure 2-2: Airborne Laser Scanning System

2.1 Airborne LiDAR systems: An in-depth Explanation

The ALS systems emit laser pulses from sensor mounted in a plane and collects information from the time-of-flight and the returned laser intensity. By the time the pulse has travelled the approximately 1-3km from the aircraft to the ground, it is roughly 20cm in width due to beam divergence. When the pulse hits an object (e.g. the forest canopy), then some of it reflects back while the rest penetrates through holes between leaves and branches. The laser pulse continues to hit structures, scattering and partially returning to the sensor until it reaches a solid barrier such as the ground and is fully blocked from further progress. The LiDAR systems record information from the backscattered laser pulse, measuring its round trip time and the returned intensity.

As mentioned at Section 1.2, there are two types of LiDAR data, discrete and FW. The discrete LiDAR observes the returned intensity signals and identifies and records a few peak intensity returns of the signal, while the FW LiDAR system digitises and stores the enitre backscattered signal into equally spaced time intervals (Figure 2-2a). The delivered data for the discrete LiDAR is a set of hit points ("returns"), which are associated with laser intensities. The world position of every return is calculated by measuring the round trip time of the laser return, giving a distance from the sensor, which is combined with the precisely known position and orientation of the aircraft/sensor (from GPS, an inertial measurement unit and precise shot direction of the laser pulse). The waveform recordings are triggered by and attached to first returns of discrete LiDAR data (to avoid sampling the uninteresting time period while the pulse travels through the atmosphere) and they are a list of intensities that correspond to the laser intensity returned over time. There is also an offset vector which defines the distance and direction between each wave sample (effectively a compression mechanism, by avoid recording the world position of every sample, replacing it with the location of the first return and this vector).

As shown in Figure 2-2b, the pulses are scanned back and forth across the landscape below (by a rotating mirror) as the plane travels forward. The scanned data has a limited maximum width according to the flight height and the field of view scan angle. During processing the track of the plane is divided into easier-to-handle pieces (flightlines) and saved into separate binary files. In this project the LAS1.3 file format is used for both datasets.

2.2 Brief Description of the LAS1.3 File Format

There are a few LiDAR file formats but the LAS1.3 was the first format to contain FW data and it is the one used to store the data for both New Forest and RedGum datasets. According to the LAS1.3 file specifications [7], a .LAS file contains information about both discrete and FW LiDAR data, with the waveform packets are attached to discrete returns and saved either internally at the end of the .LAS file or externally in a .WVS file.

As shown at (Figure 2-3) the .LAS file is divided into four sections and a brief explanation of each section is given here:

1. The **Header** contains general information about the entire flightline. For example, it includes the maximum scan angle used during the flight, whether the waveform packets are recorded internally or externally and the number of **Variable Length Records** (VLR).

2. Regarding the **VLR**, which contain arbitrary "extension" data blocks, the most important information given is the waveform packet descriptors that contain essential information on how to read the waveform packets (i.e. an ID, the number of wave samples and the size of each intensity in bits).

3. The **Point Data Records** are the discrete points and the waveforms are associated with first return discrete points. Each Point Data Record has a spatial location, an intensity and optionally a pointer to a waveform packet as well as the ID of the corresponding waveform packet descriptor.

4. The waveform packets is a list of intensities and they are either saved internally into the **Extended Variable Length Records** section of the .LAS file or inside an external .WVS file. Starting from the associated first return point, the spatial locations of the waveform packet (wave sample intensity) are calculated by adding an offset defined in the associated Point Data Record.

2.3 Leica Vs Trimble Instruments: Limitations, Differences and Advantages

As shown in Figure 2-1, the Leica ALS 50-II instrument was used to capture the LiDAR data of New Forest dataset and the Trimble AX60 for collecting the RedGum Forest FW LiDAR data. It is therefore important to clarify the differences, the limitations and the advantages of each instrument.

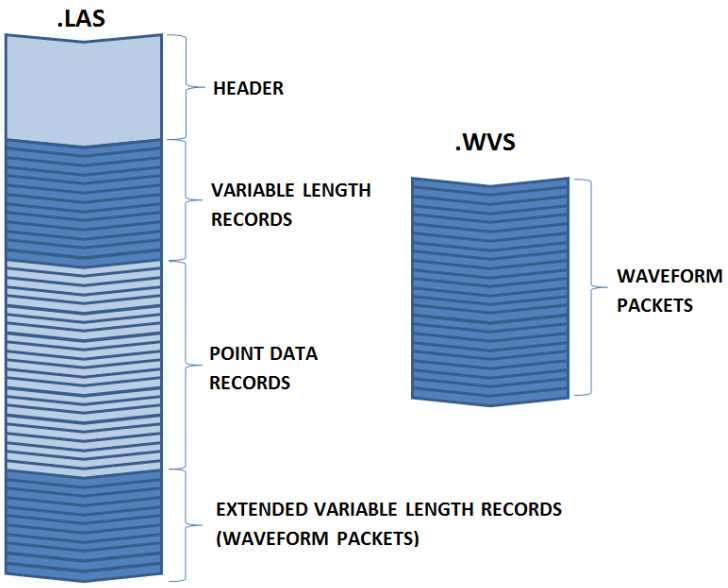

Figure 2-3: How the FW LiDAR data are stored into a binary file, according to the LAS1.3 file format specification

The Trimble performs at a pulse frequency of 400kHz, while the Leica's maximum pulse frequency is 120kHz. Nevertheless, during experiments there were occasions when the Leica discarded every other waveform due to I/O limitations despite being at or below the maximum pulse frequency [8]. The New Forest dataset has been affected by this and, on average, one third of the saved pulses only contain discrete data. We should therefore be extremely careful when comparing Discrete with FW LiDAR data. While [5] concludes that FW LiDAR data worth the extra processing because they have a better vertical profile, [9] states that extra information (the echo-width) from the FW LiDAR data are relatively unimportant. But the New Forest datasets were used for the comparison at [9] and there is no mention about the significantly less waveforms recorded in comparison to the discrete data. It is therefore suspected that their results has been affected by the missing waveforms.

Another problem with the Leica sysyem is the small dynamic range of intensities due to the number of bits used for recording them; the Leica system uses 8-bit integers (0-255 range) while the Trimble uses 16-bit integers (0-16385 range). For increased dynamic range and finer intensities without doubling storage costs, Leica introduced an Automatic Gain Controller (AGC). The AGC is an 8-bit number that defines how the recorded intensity range is shifted across a wider range of intensities. The AGC value is adjusted according to the reflected laser intensity of the previous 64 pulses and it therefore varies across a flightline. Consequently, the raw intensities are incomparable

to each other and, since the relation between AGC and the intensities is not linear, the range normalisation is complicated [10] [11]. In this thesis, the intensities of the Leica system are used as boolean values (whether something existed or not, using a user-defined threshold) to quickly overcome that issue and focus on the major research objectives. Regarding the Trimble instrument, there is no AGC value because the intensities are saved into a 16bit integer and as long as the flight height is constant no normalisation is required. In a few words, the raw intensities recorded using the Leica system are not normalised and therefore not comparable to each other, while the intensities of the Trimble instrument are more meaningful.

The footprint of the laser on the ground depends on the scanning pattern of the instruments and the field of view. The sinusoidal scanning pattern of the Leica system results in a higher density of returns at the edges of the flightline. The footprint of the Trimble instrument is more equally spaced because they are scanned using a rotating polygon. The uneven density pattern of the Leica system is resolved by normalisation during the voxelisation process, but the Trimble's equally spaced pulse pattern is more prone to aliasing when voxelised. Regarding the field of view, the Leica is wider but both systems avoid large angles because otherwise data look deformed at edges of the flightlines.

Last but not least, the Trimble instrument is a native full-waveform sensor; the discrete LiDAR are produced by extracting peak points in post-processing. Therefore one of the purported advantages of a FW system, the concept of extracting a denser point clouds using Gaussian decomposition [2], does not apply in the Trimble's case. This was proven by extracting peak points from Trimble FW LiDAR data using the pulseextract from LAStools [12]; the number of points extracted was exactly the same as the number of points saved into the associated discrete LiDAR files. Therefore discrete data from the Trimble instrument are the same as those generated by echo decomposition and peak points extraction from the FW samples.

To sum up, the Trimble AX60 instrument is a newer sensor and therefore has less problems or design compromises in comparison to the Leica ALS50-II instrument. Table 2.1 summarises the differences between the two sensors.

2.4 Hyperspectral Imagery

Hyperspectral imagery has a positive impact in remote sensing because it contains information beyond human visibility. The human eye receives light from the visual spectrum into three bands (red, green and blue). The hyperspectral sensors captures a larger spectrum and divides its light components into hundreds of bands, recording

Table 2.1: Specifications of the LiDAR instruments used

Instrument Name:	**Leica ALS550-II**	**Trimble Ax60**
Scanned Area	New Forest, UK	RedGum, Australia
Year of Introduction:	Discrete LiDAR 2009 & FW LiDAR 2010	2013
Max Scan Frequency (kHz):	120	400
Recorded Intensity (bits):	8	16
AGC:	Yes	No
Scanning Pattern:	Sinusoidal	The footprints are more equally spaced on the ground
Max field of view (degrees):	75	60

this way more information than a human eye can receive [1].

Nevertheless, there are other compromises - for example, the time taken to integrate incoming light as the aircraft carrying the sensors moves. This means the raw airborne images appear deformed because the pixel length varies across the flightline. NERC-ARF geo-corrects the data using the Airborne Processing Library (APL) [13]. The processing levels are numbered. At 'level 3' (world coordinate system) the pixels are equally spaced and sized, which requires resampling and thus may look slightly blurred. The 'level 1' data (what the sensor saw) are non geo-corrected but they are associated with a file that defines the spatial location of each pixel. In this thesis, the 'level 1' data are used to preserve the highest possible quality.

In practise, the level 1 data are held in two files, the '.bil' and the '.igm'. The '.bil' file contains the hyperpsectral cube (Figure 2-4), all the pixel values at different wavelengths, and the .igm file gives the x, y, z coordinates of each pixel.

The number of bands and the spectrum range captured depends on the hyperspectral sensor. The data from New Forest were collected using the following instruments:

- the Eagle, which captures the visible and near infra-red spectrum (400-970nm)
- the Hawk, which covers short wave infra-red wavelengths (970-2450nm)

Both sensors divide their spectral range into 252 bands (programmable) and each band is a 2D vector as shown in Figure 2-4).

The hyperspectral images also come with a number of drawbacks. A few are mentioned here but since hyperpsectral imagery is not the main focused of the thesis there are not addressed:

- System faults sometimes occurs and the affected areas are masked out. This results in blank areas.

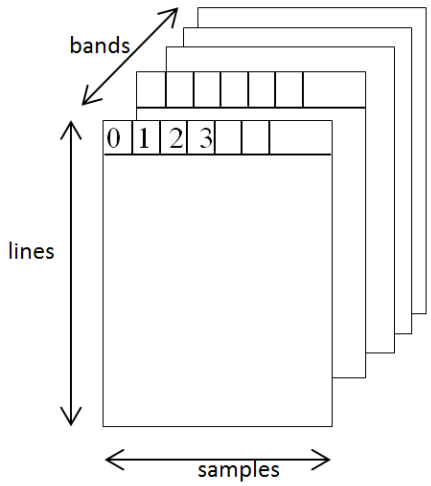

Figure 2-4: This figure shows the order of the hyperspectral pixels saved into the the binary .bil file.

- As a passive sensor, it is dependent on the sun for illumination and thus vulnerable to poor weather conditions
- Due to the high refraction of light at some wavelengths, some bands are highly influenced by humidity (i.e. wavelength 1898.33nm).

To sum up, hyperpsectral images contain information beyond the visible and they are delivered in two files, one contains the hyperspectral cube and the other one the geo-locations of each pixel. In this project, they are used in chapter (Chapter 7), where it is shown that the combination of Remote Sensing data confers better results for generating tree coverage maps.

Chapter 3

Overview of Thesis

Chapter 4

The open source software DASOS and the Voxelisation Approach

Chapter 5

Surface Reconstruction from Voxelised FW LiDAR Data

Chapter 6

Optimisation Attempts for the Surface Reconstruction

6.1 Problem and Challenges

While Section 5 explains a simple approach of extracting a polygonal surface from the voxelised FW LiDAR data, this section is mainly focused on objective No. 5 from table (**??**); it tests the performance of six different data structures on the surface reconstruction and it attempts to improve the interpretation of volumetric data by introducing new data structures. The main challenges raised for this task are because the input data is real laser scanning data that contains noise. Some of the challenges that this chapter attempts to tackle are listed below:

1. The LiDAR sensors are vulnerable to clouds and seagulls being misinterpreted and recorded as hit points. Those outliers are much higher than tree canopies but they are within the boundaries of the scanned area. As a result, on average 97.5% of the voxels are empty.

2. The Marching Cube, as described in Section **??**, is a scan line algorithm, which implies looping through every single voxel, including the empty ones. This is very time consuming and therefore, algorithms that quickly identify and ignore empty areas are essential.

3. While loading an entire volume, the huge amount of empty voxels may lead into exceed memory usage. It is therefore preferable to store the voxels into structure that avoids storing the empty ones (i.e. hierarchically).

4. When extracting a surface from real data, it is very likely to generate non-manifold objects. Non-manifold objects are not homeomorphic to Euclidean 1-space be-

cause they have crossing points. This also occurs at the polygonal meshes generated by DASOS as explained at Chapter 5.

***NEILL: I would make these comments higher level until you have explained more in the chapter.

6.2 Related work

6.2.1 Full-Waveform LiDAR Visualisation

Summarising previous aforemonetioned related work (Section **??**), traditional ways of interpreting the full-waveform LiDAR data suggest echo decomposition for detecting peak points and interpreting the point clouds extracted [14]. Both SPDlib [19] and FullAnalyse [18] visualises either the peak extracted points or the raw waveform samples. On the one hand, SPDlib visulises the samples as points with intensity above a given threshold, while FullAnalyse generates a sphere with radius directly correlated to that intensity of each wave sample. Similarly, Pulsewaves visualises a number of waveforms with different transparency according to their intensity [17]. On the one hand, visualising all the wave samples makes understanding of data difficult due to the high noise. On the other hand, peak point extraction identifies significant features but the FW LiDAR data also contains information about echo widths. These information can be accumulated from multiple shots into a voxel array, building up a 3D discrete density volume [23].

Voxelisation of FW LiDAR data was introduced by [20] who used it to visualise small scanned areas (15mx15m). The waveforms samples were inserted into a 3D Voxelised space and the voxels were visualised using different transparencies according to their intensity. Similarly, as explained at Section **??**, we adopt voxelisation for surface reconstruction and applied it on larger areas. Once the 3D density volume is generated, numerical implicitisation is used to represent the scanned area. Nevertheless, visualising numerical/implicit objects is not straight forward, since they contain no discrete values (Section **??**). This problem can either be address by ray-tracing [27] or polygonisation [33]. In this thesis, the polygonisation direction is taken and a simple approach is explained in Section **??**. This chapter introduces new ways of interpreting real voxelised data and tests how well six data structures and algorithms perform on surface reconstruction.

6.2.2 Optimising Volumetric Iso-surface Extraction

Even though volumetric visualisation has only been recently used for FW LiDAR systems, there are many applications in medical visualisation [?] [?] and visual effects [30] [?]. Research work exists on optimising both ray-tracing and surface reconstruction and it can be categorised into three groups: surface-tracking, parallelisation and data structures. Those approaches are discussed below along with their benefits and limitations with respect to voxelised FW LiDAR data.

Surface-tracking was applied at Rodrigues de Araujo and Pires Jorge [?] and Hartmann [?]. Starting from a seed point, the surface is expanded according to the local curvature of the implicit object. This method is considered to be faster and more efficient in comparison to the Marching Cubes algorithm since huge empty spaces are ignored. It further opens up possibilities for finer surface reconstruction at areas with high gradient changes. Nevertheless, surface-tracking algorithms cannot be applied with real laser scanning data because these data are neither manifold nor closed. For example, in a forest scene, a tree canopy may be detached from the ground due to missing information about its trunk. Therefore, by tracking the surface, the algorithm may converged at a single tree instead of the entire forest.

Hansen and Hinker proposed parallelising the polygonisation process of BlobTree trees on Single Instruction, Multiple Data (SIMD) machines [?]. The Instruction is a series of commands to be executed. The longer the series of the commands is, the greater the speed up is. BlobTree trees represent implicit objects as a combination of primitives and operations [?]. While the depth of the tree increases, the length of the parallelised instruction increases as well and therefore good speed up is achieved. Nevertheless the function at the implicit representation of the FW LiDAR data at [23] is executed at constant time, making it harder to achieve speed up using SIMD machines. Further, according to the C++ Coding Standards when optimisation is required is better to seek an algorithmic approach first because it is simpler to maintain and less likely to contain bugs [?].

Hierarchical data structures, like octrees, improves the performance of the isosurface extraction because of the huge amount of empty voxels that can be ignored during polygonisation [?]. The literature in the data structures direction aims to either simplify/improve the output mesh, optimise traversal time of hierarchical data structures or eliminate hierarchy. For example, the extraction of locally finer details either with dual grids [?] or edge-trees [?] reduces the amount of vertices produced. In addition, a net of linked surface nodes improved anti-aliasing and reduces artifacts of 3D Magnetic Resonance Imaging (MRI) [?]. Regarding efficiency of accessing data, franctional cascading slightly improved time complexity of range queries [?]. Sparse Voxel Octrees

improved efficiency by having a pointer pointing to children and packing children coherently in memory [**?**]. Hadwiger et al. used a 3D virtual memory to keep voxels coherent on GPU and avoid traversal [**?**]. Nevertheless, due to the adjacency of neighbouring voxels, data are saved for empty voxels yielding into much wasted memory. OpenVDB library arranges blocks of grids into a B+ hierarchical data structure for increased cache coherency and lower tree depth [**?**]. The bricks stuctured used at GigaVoxels is similar in terms of blocks, named bricks, and it's been used for efficient GPU ray-casting [30]. For eliminating tree traversal time, Warren and Salmon introduced hash octrees for N-bosy simulation of particles [**?**]. Similarly, voxel hashing was proposed for overheading the traversal time of hierarchical structures and real time surface reconstruction using depth cameras online [**?**]. Most of those data structure optimisations are based on GPU processing, but they are still very relevant.

6.3 Overview

This thesis compares six approaches for handling and polygonising voxelised full-waveform LiDAR data. The first three approaches use data structures from the literature and the scan line Marching Cubes algorithm. An explanation of their functionalities is given at Table 6.1. The last three approaches are more complicated because they take into consideration the chunks of empty voxels and ignore them during surface reconstruction. A brief summary of them is given in Table 6.2 and an in-depth explanation is given in Sections 6.4 6.5 6.6 . Please note that the "1D Array" is the original implementation, while each one of the other five approaches tackles at least one of the aforementioned challenges (Section 6.1).

1D Array	Voxel Hashing	Octree
Influenced by [?], all the data are saved into an 1D array to guarantee coherent memory, even though much memory is wasted in regards of empty voxels.	The intensities of the voxels are saved into a simple hash table with key value relevant to their position into the volume. Similary to [?], this approach overheads traversing time of hierarchical structures and on top of that it reduces memory allocation because empty voxels are not stored.	This is a hierarchical octree with traversal time to be essential. Please note that this is a scan line test and therefore it does not take into consideration empty chunks of memory.

Table 6.1: Brief Description of the Three Scan-Line Tests

Integral Volumes	Octree Max and Min	Integral Tree
This data structure is an extension of 'Integral Images' to 3D. It was firstly presented at the CGVC conference as part of this thesis. Using Integral Volumes, the sum of any cuboid area is calculated in constant time. By repeatedly dividing the space into cuboids, big empty spaces are quickly identified and ignored during the surface reconstruction. (Section 6.4)	In this approach, the values are saved into an octree, but the surface reconstruction is build along the tree. This is slightly different than a traditional octree, because at each branch node its max and min values are saved. This way, areas that are completely full or empty are identified during traversal before reaching the leaves of the trees. (Section 6.5)	It is a combination of octree and integral volumes; the sum of a given branch is given at constant time. That was an attempt to combine the idea of 'Integral Images' and octrees. Nevertheless, traversal time and backtracking for finding neighbouring voxels still exists. (Section 6.6)

Table 6.2: Description of the Three Optimisation Attempts

6.4 Integral Volumes

The 'Integral Volumes' optimisation is based on the idea of Integral Images, which is an image representation where each pixel value is replaced by the sum of all the pixels that belong to the rectangle defined by the lower left corner of the image and the pixel of interest. An integral image is constructed in linear time and the sum of every rectangular area is calculated in constant time, as shown in figure 6-1 [**?**]

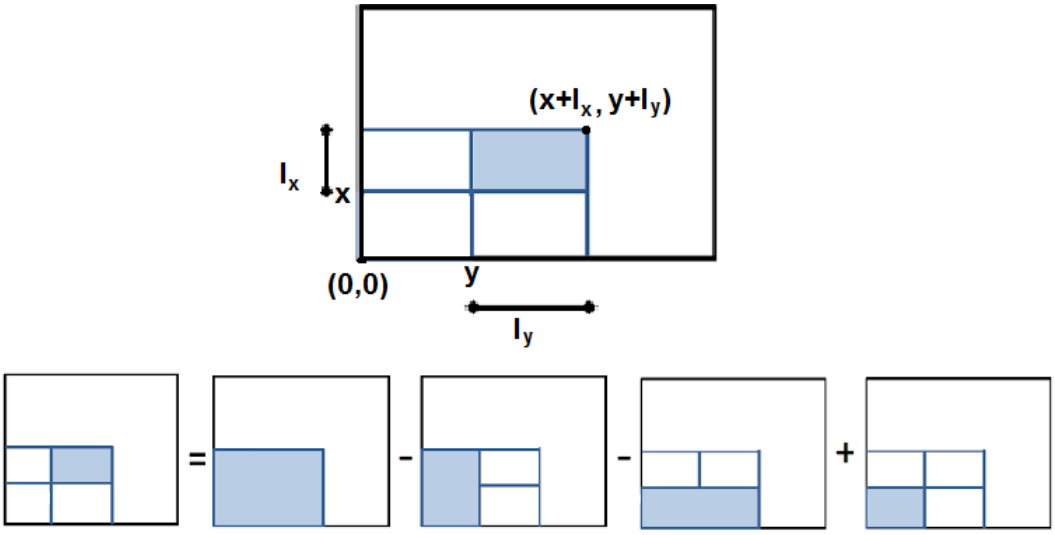

Figure 6-1: Once the Integral Image is constructed, the sum of any rectangular area is calculated in constant time.

In this paper, we extend 'Integral Images' to 'Integral Volumes' and use them to quickly identify and ignore big chunks of empty voxels during polygonisation. The following section explains the mathematics behind 'Integral Volumes', while sections 6.4.2 and 6.4.3 give an in depth description about the algorithms invented.

6.4.1 Extending Integral Images to Integral Volumes

As shown in Figure 6-1,the area of interest is defined by the pixels (x, y) and $(x+l_x, y+l_y)$ and the sum S is given by:

$$\begin{aligned} S =& T(x + l_x, y + l_y) - T(x + l_x, y - 1) - \\ & T(x - 1, y + l_y) + T(x - 1, y - 1) \end{aligned} \tag{6.1}$$

where S is the sum of rectangular area of interest, $T(x, y)$ is the value of the integral image at (x, y) and l_x, l_y define the length of the rectangle in the x and y axis respectively.

Extending integral images to 3D, the value of the voxel (x, y, z) in a 3D integral volume becomes equal to the sum of all the values that belong to the box defined by the (x, y, z) and $(0, 0, 0)$ included. Therefore the sum (S) of the box defined by (x, y, z) and $(x + l_x, y + l_y, z + l_z)$ included is given by:

$$\begin{aligned} S = & T(x - l_x, y + l_y, z + l_z) - T(x - 1, y + l_y, z + l_z) - \\ & T(x + l_x, y - 1, z + l_z) - T(x + l_x, y + l_y, z - 1) + \\ & T(x - 1, y - 1, z + l_z) + T(x - 1, y + l_y, z - 1) + \\ & T(x + l_x, y - 1, z - 1) - T(x - 1, y - 1, z - 1) \end{aligned} \tag{6.2}$$

where $T(x, y, z)$ is the value of the voxel (x, y, z) in the 3D integral volume. S is the sum of voxels inside the box, $T(x, y, z)$ is the value of the voxel (x, y, z) in the 3D integral volume. and l_x, l_y, l_z define the length of the box in the x, y and z axis respectively.

6.4.2 Optimisation Algorithm

As mentioned before, using 'Integral volumes' empty areas are quickly identified and ignored during polygonisation. An iterative algorithm is introduced here. This algorithm continuously splits the volume and checks whether the sub-volumes and its neighbouring voxels are empty using the 'Integral Volumes'. Please note that all the values below the threshold boundary of the object must be zero and all the non-empty voxels must contain a positive value.

Algorithm 1 Integral Volumes Optimisation Algorithm

```
1: Push the entire Volume as a cuboid inside a Stack
2: while stack is not empty do
3:     Cuboid-A ← next cuboid from the Stack
4:     if Cuboid-A and neighbours are empty then
5:         discard Cuboid-A
6:     else if Cuboid-A consists of only one cube then
7:         polygonise Cuboid-A
8:     else
9:         divide Cuboid-A
10:        push the two new Cuboids into stack
```

Here it is worth highlighting that, on line 3 of the algorithm it is checked if the neighbouring cubes of a cuboid are empty, because the voxels of the 3D density volume and the cubes in marching cubes algorithm are aligned with an offset (Figure **??**). If volumes with non-empty neighbouring voxels are ignored, then holes appear on the

output polygon mesh.

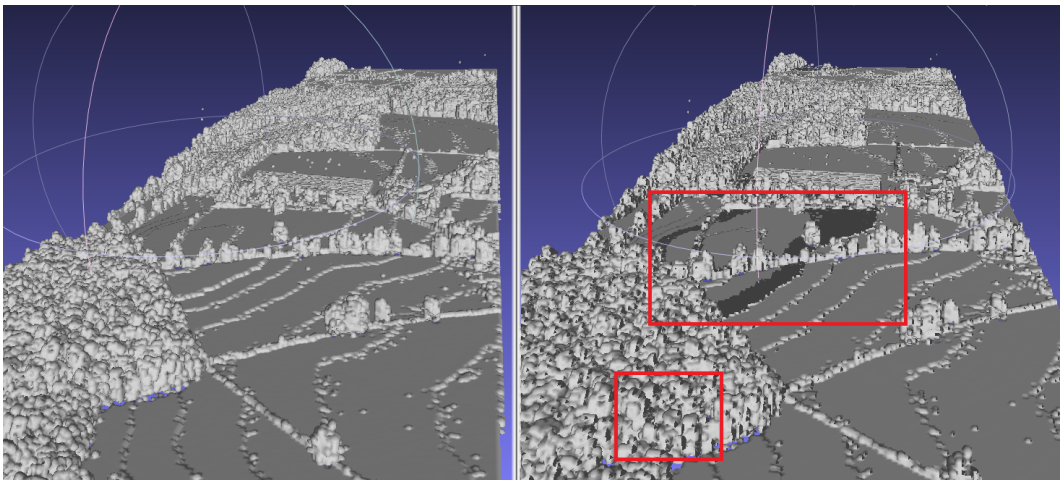

Figure 6-2: Comparison between including and ignoring neighbouring voxels; holes appears when ignored. Inside the red boxes, there are two affected areas.

6.4.3 Coding Details for Faster Implementation

Implementation details contributes to the efficiency and speed up of the algorithm. Significant improvements are achieved by reducing recursions, big memory allocations and if statements, since memory jumps are time expensive. As shown in algorithm 1, a while loop is used to avoid recursion. In this section it's given an explanation on how the stack controls memory consumption and how bitwise operations reduces if-statement usage.

Regarding memory consumption, a stack was chosen over a queue, to decrease the amount of cubes saved into the data structure simultaneously. A queue is a first in first out data structure, while a stack accesses data in a last in first out order. In every iteration, it is ideal to interpret the smallest saved cube, such that the possibility of being polygonised is higher and the possibility of storing another cube is less. A queue guarantees cubes with approximately the same size, since the big cubes will be added first and sequentially being divided first. In contrast, a stack guarantees the smallest possible number of cubes saved. The larger cubes are stored in the bottom of the stack while the smaller ones are interpreted first because they are always the last one divided and inserted into the stack. For that reason, a stack guarantees the lowest memory usage.

Furthermore, in algorithm 1 an issue exists: how to quickly identify the side to be divided next? Ideally, the usage of if-statements should be low because they contains

many time expensive memory jumps. For that reason, bitwise operations were embedded into the program to reduce their usage. A cube is defined with its position, its size, the next side to be divided s and its divisible sides D. The parameter s takes the values 1, 2, 3 for the x, y, z sides respectively. The parameter D is an integer consisting of the sum of three numbers (1 or 0) + (2 or 0) + (4 or 0) indicating whether the sides x, y, z are divisible or not (table 6.3). The parameter D takes the value between $[0, 7]$ and covering all the possible cases of divisible sides as shown in tables 6.4 and 6.5. For example if x and z are the divisible sides, then $D = 1 + 0 + 4 = 5$. By the end, the bitwise operations and the faster implementations of the Integral Volumes optimisations is shown at algorithm 2.

	Decimal Numbers		Binary Numbers	
Side	Divisible	Not Divisible	Divisible	Not Divisible
X	1	0	0001	0000
Y	2	0	0010	0000
Z	4	0	0100	0000

Table 6.3: Values of divisible sides

X	1	-	1	-	1	-	1	-
Y	2	2	-	-	2	2	-	-
Z	4	4	4	4	-	-	-	-
D	7	6	5	4	3	2	1	0

Table 6.4: How to calculate the value of D, which represents the divisible sides of a cuboid

X	0001	-	0001	-	0001	-	0001	-
Y	0010	0010	-	-	0010	0010	-	-
Z	0100	0100	0100	0100	-	-	-	-
D	0111	0110	0101	0100	0011	0010	0001	0000

Table 6.5: How to calculate the value of divisible sides (D) in binary representation

Algorithm 2 Integral Volumes Optimisation Algorithm

```
1: Push the entire Volume as a cuboid inside a Stack
2: while stack is not empty do
3:     Cuboid-A ← next cuboid from the Stack
4:     if Cuboid-A and neighbours are empty then
5:         discard Cuboid-A
6:     else if D is equal to 0 then
7:         polygonise Cuboid-A
8:     else if (D bitwise add 2^s) shift right (s − 1) then
9:         divide side s of Cuboid-A
10:        if the new length of side s is equal to 1 then
11:            D ← D bitwise add (7 − 2^s)
12:        s ← (s + 1) mod 3
13:        push both new Cuboids into stack
14:    else
15:        s ← (s + 1) mod 3
16:        push Cuboid-A back into the stack
```

6.5 Octree Max and Min

'Integral Volumes' quickly identify and ignore empty spaces during polygonisation (tackles the 1st, 2nd and 4th problem of the original algorithm – Section 6.1), but it allocates memory for the entire volume (the 3rd problem). For that reason, the 'Octree Max and Min' data structure has been implemented.

The 'Octree Max and Min' data structure avoids storing empty voxels and it also identifies empty areas during polygonisation. The polygonisation is built on the traversal of the octree, as explained in Algorithm 3. Similarly to 'Integral Volumes', a stack is used to avoid recursion and reduce memory jumps. When the 'Integral volumes' are used, it is checked whether the neighbours of a cuboid and itself are empty or not. If they are both empty then the cuboid is ignored. The neighbouring voxels have to be checked in order to avoid generating holes on the polygonal mesh. Similalry, it is essential to check neighbouring voxels when a branch of the 'Octree Max and Min' data structure is ignored. Nevertheless, because the branches of the octree are always a cube, it is not trivial to check whether they are empty or not. For that reason, if a branch is empty then we loop through its edges and polygonise them according to look up table of the the Marching Cubes algorithm.

Embedding the polygonisation of volumetric data into an octree has been done before [**?**]. Nevertheless, the 'Octree Max and Mean' data structure differs in two ways:

- The max and min values of each branch are stored into the corresponding node

Algorithm 3 Embedding the Marching Cubes Algorithm into an octree structure

```
1: Push the Root as a Node into a Stack
2: while stack is not empty do
3:     Node-N ← next Node from the Stack
4:     if Node-N is a Leaf then
5:         polygonise Leaf
6:     else if Node-N has no children OR max value of Node-N < isolevel
   OR min value of Node-N > isolevel then
7:         Polygonise edges of cubic with root node-N
8:     else
9:         push the children of Node-N into the Stack
```

to speed up polygonisation. This enables checking whether the leaves of a branch lie either only inside or only outside the implicit object[1]. If they do, then no iso-surface is crossing that branch and it can be discarded (after polygonising its edges).

- A new algorithm is proposed and implemented for finding neighbouring voxels. This algorithm reduces comparisons and jumps in memory. An in-depth explanation of this algorithm is given at Section 6.5.1.

6.5.1 Finding Neighbours

Every time a voxel/leaf is polygonised, seven of its neighbours are checked to decide whether a surface is passing through that area or not. At hierarchical data structures, the nearest common ancestor is tracked upwards and the branch, with root the common ancestor, is traversed to reach the neighbour. The article [**?**] uses recursion that terminates once a common ancestor between a leaf and its neighbour is identified. According to Scharack [**?**], finding neighbours in linear octree[2] is done in constant time. Nevertheless, linear octrees are full octrees. Therefore, if used in our case all the empty voxels would have to be stored as well. Lohner suggested vectorising the space during post-processing for finding the shortest distance between un-constructed points [**?**]. However, the 3D voxelised FW LiDAR is a regular grid and during polygonisation the shorter distance to travel is one voxel. For that reason, simpler approaches with less initialisation time, like [**?**], could perform equally well. Castro et al. [**?**] assume that with hierarchical octrees it is not possible to start searching neighbours from leaves and suggest using hashed octrees to do that. In contrast, it is possible to start from the leaves and find the common ancestor using parentship as described at [**?**].

[1] Explanation about implicit/algebraic objects is given at Section **??**

[2] Linear octrees are octrees whose leaf nodes are stored into a linear array.

To avoid recursion and reduce comparison, this thesis introduces a new way of finding the common ancestor using logarithms of 2. The Algorithm 4 explains the proposed method. As shown in Figure 6-3, there are occasions where it is cheaper to start searching a neighbour from the root instead of the leaf. For example Node-F is the (+1) neighbour of Node-E. If we start looking for it from the leaves then we need to travel through 6 nodes, but if we start from the root we only need to travel 5 nodes. Logarithms helps us decide which route to take, while reducing comparisons since it is not required to check whether branches has common faces while travelling upwards [**?**].

Algorithm 4 Finding the number of steps required to go upward in order to find the common ancestor of a Leaf(x) of interest and its (+1) neighbour

$c \leftarrow \text{ceil}(log_2 x)$
$c_1 \leftarrow \text{ceil}(log_2(x+1))$
while $c = c_1$ **do**
    $x = x - 2^{(c-1)}$
    $c \leftarrow \text{ceil}(log_2 x)$
    $c_1 \leftarrow \text{ceil}(log_2(x+1))$
if $D_{max}/2 < c_1$ **then**
    Start from Root to find Neighbour Branch +1
else
    Backtrack c_1 parents to find the common ancestor
    Find neighbour

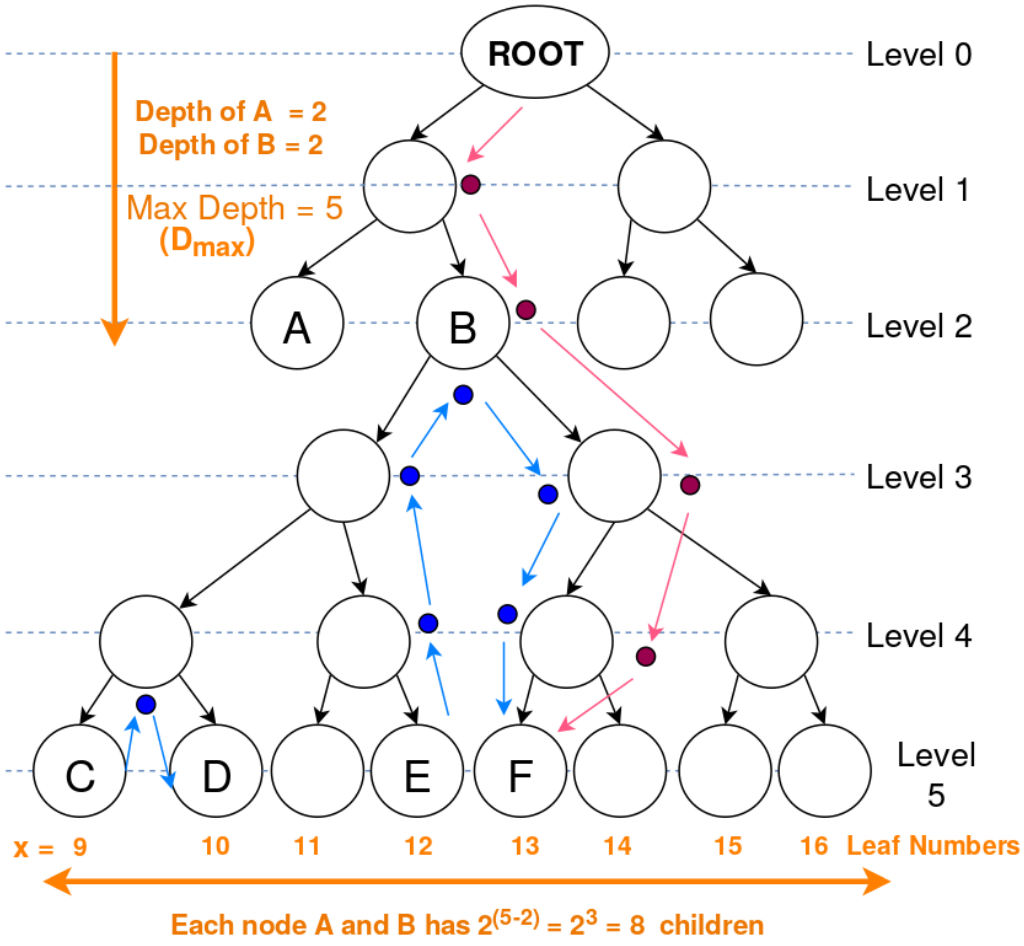

Figure 6-3: This diagram depicts the parameters used for finding neighbouring voxels.

6.6 Integral Tree

6.6.1 Main Idea

The 'Integral Tree' is a new term that describes the attempt to preserve some properties of the 'Integral Images' while using a non-full tree structure. Every 'Integral Tree' consists of two elements: an integral 1D-array and a tree. All the values of every non-empty and non-connecting node are saved into an 1D-array, in a way such that the condition of the 'Integral Tree' is fulfilled: all the values of every branch B are adjacent inside the 1D-array. Afterwards the array is converted to integral; the sum of every n continuous values is calculated in constant time. Additionally, the root node of each branch B contains two parameters $(*p, k)$. The number k is the number of nodes, which contain values, of the branch B (e.g. for an octree, it is all its leaf nodes) and the pointer $*p$ points to the first one in the 1D-array (Figure 6-4).

*** NELL:: the *p is a pointer)

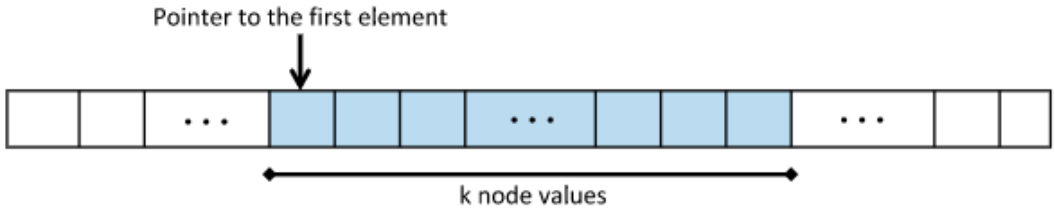

Figure 6-4: Ordering of tree elements

The aforementioned rules can be applied to any tree structures including binary trees, quadtrees and octrees. To better perceive how this data structure works, let's assume that there is a number of 2D spatially distributed values. Figure 6-5 depicts how they can be saved into an 'Integral Quad Tree' in order to fulfil the adjacency condition of the 'Integral Tree'. Also, Section 6.6.2 gives an example of an 'Integral Binary Tree'.

6.6.2 Integral Binary Tree Example

An example of applying the idea of 'Integral Tree' into a binary tree is given for clarification (Figure 6-6). Firstly, the values of the binary tree are sorted into the 1D-array A as {15, 12, 10, 13, 14, 17, 16, 18, 19} in order to fulfil the adjacency condition. Secondly, the array A is modified as {15, 27, 37, 50, 64, 81, 97, 115, 134} in order to become integral using the following equation:

$$A[i] = A[i] + A[i-1] \tag{6.3}$$

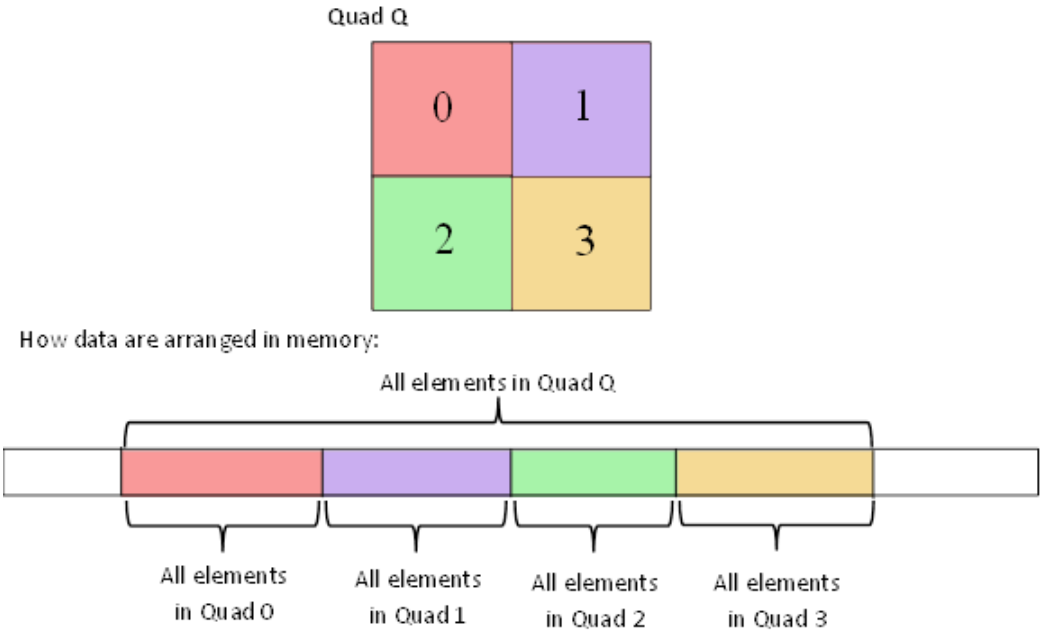

Figure 6-5: Illustration of how to save the values of an 'Integral Quad Tree' into the 1D-array, in order to preserve the condition of 'Integral Trees'

*p	0	1	2	3	4	5	6	7	8
1-D Array (1st step)	15	12	10	13	14	17	16	18	19
1-D Array (2nd step)	15	27	37	50	64	81	97	115	134

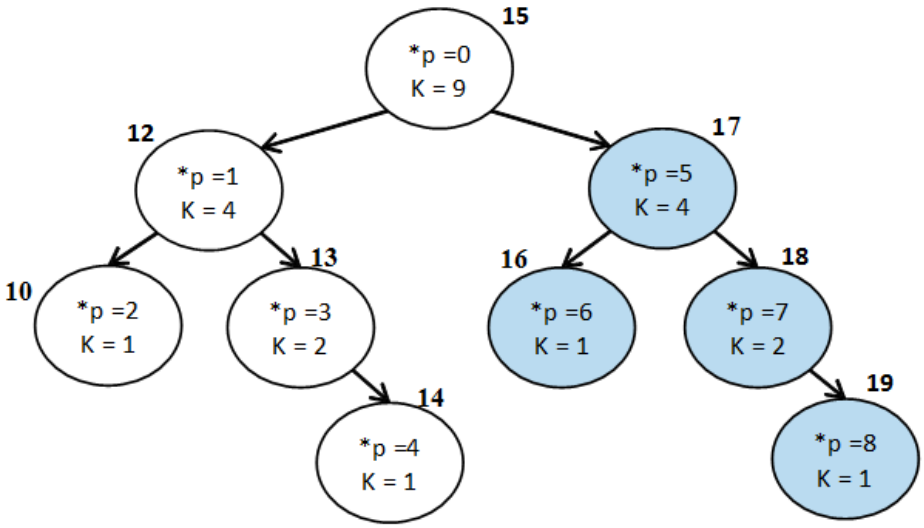

Figure 6-6: Example of 'Integral Binary Tree'

Then the sum S of a branch, with $(*p,\ k)$ parameters, is calculated at constant time as follow:

$$S = A[*p + k - 1] - A[*p - 1] \tag{6.4}$$

For instance the sum of the blue branch on Figure 6-6 is $A[5 + 4 - 1] - A[5 - 1] = A[8] - A[4] = 134 - 64 = 70$, which is correct since $17 + 16 + 18 + 19 = 70$.

6.6.3 Integral Octree for Surface Reconstruction

For an 'Integral Octree', all the values saved into the integral 1D-array are the values of the leaf nodes since the rest are connecting nodes. For the surface reconstruction, an 'Integral Octree' is implemented and the same polygonisation algorithm as 'Octree Max and Min' are used (Algorithm 3 and Algorithm 4). The only difference is the comparison at Line 6 of Algorithm 3; instead of checking the max and min values, the sum of the branch is checked instead. If the sum is smaller than the iso-surface value then no surface is crossing that area and the branch is discarded.

6.7 Data Structures Summary

To briefly sum up, the following six data structures has been implemented their performance has been tested for reconstructing polygonal meshes from voxelised FW LiDAR data:

1. **1D-Array**: Simple array that keeps data coherent in memory for quick access.
2. **Voxel Hashing**: A hashed table is used for storing the intensity values of the voxels [**?**].
3. **Octree**: Simple hierarchical structure with a scan-line implementation.
4. **Integral Volumes**: Extension of 'Integral Images' that allows finding the sum of any cuboid area in constant time. It is a new algorithm and it is used for quickly identifying and ignoring empty areas during polygonisation.
5. **Octree Max/Min**: The polygonisation is embedded into an hierarchical data structure [**?**]. The max and min values of each branch are stored to identify and ignore branches that either only contain low level noise or are completely inside the implicit object. Logarithms are further introduced for faster neighbouring finding.

6. **Integral Octree**: An attempt to preserve properties from both 'Octree Max/Min' and 'Integral Volumes'.

Each one of the aforementioned data structure has different properties and attempts to address at least one of the problems mentioned in Section 6.1. The first three implementations are scaline algorithms, which means that polygonisation is linear and all the voxels, including the empty ones, are checked for generating triangles primitives. Some data structures are taken from the literature to test how well they perform on this specific datasets while others are new and presented into this thesis. Table 6.6 summarises their properties and the problems each data structure attempts to resolve.

***Neill: Include citations in table for existing scanline algorithms from literature

	Scan-line algorithm: loops through all voxels (1)	Identifies and ignores empty areas during polygonisation (2)	Avoids storing empty voxels in memory (3)	Works on non-manifold objects (4)	Requires Cubic Boundaries of the voxelised data	New data structure, introduced for this thesis
1D-Array	✓	-	-	✓	-	-
Voxel Hashing	✓	-	-	✓	-	-
Octree	✓	-	✓	✓	✓	-
Integral Volumes	-	✓	-	✓	-	✓
Octree Max/Min	-	✓	✓	✓	✓	✓[3]
Integral Octree	-	✓	✓	✓	✓	✓

Table 6.6: Summarising the addressed challenges and the properties of all the data structures implemented.The numbers of the first four columns correspond to the challenges described in Section 6.1

6.8 Results and Testing

The implemented algorithms are beneficial in different aspects: speeding up execution or decreasing memory usage. The performance has been tested within two groups of test cases:

[3]Integrating polygonisation into an octree has been done before, but there only a few modifications to a normal octree; the max and min values stored into the branch and the introduction of logarithms for finding neighouring voxels.

- The results of the first group are given in Table 6.7 and visualised in the Charts depicted in Figures 6-7, 6-8, 6-9 and 6-10
- The results of the second group are given in Table 6.8. The related charts are inside Table 6.9.

This section clarifies the various parameters of testing, while the following Section 6.9 discussed the results and explains the behaviour of the algorithms in respect to the results.

The two test cases has only one difference, while the rest of the parameters are the same. The difference is that the first one uses one flightline (the LDR-FW-FW10_01-201009821.LAS from New Forest) and focuses on its performance using a finer resolution range. In contrast, the second uses three filghtlines from the NERC-ARF datasets. The 1st flightline is from the New Forest (LDR-FW-FW10_01-201009822.LAS), the 2nd flightline is from the Dennys Wood (LDR-FW10_01-201018713.LAS) and the 3rd one from Eaves Wood (LDR-FW-GB12_04-2014-083-13.LAS). The 2nd group checks whether there are significant performance differences when the algorithms are applied on different fligtlines.

Except from the flightlines used, the rest of the parameters are the same in both test cases. In order to understand the size of the data, the voxel length, the number of voxels in the x,y,z axes and the percentage of empty voxels are stated. The smaller the voxel length is, the more voxels exist because the boundaries of the voxels in meters are constant and when the voxel length decreases the resolution of the volume increases. Additionally, for every resolution the execution time and maximum memory consumption are measured. Execution time is further divided into data structure construction (including reading the LAS file) and polygonisation.

*** Neill::: Consider adding log(execution time) in diagrams and sum of voxels per test in the results

			1D-Array				**Voxels Hashing**				**Octree**			
Specifications			Time (s)			Memory	Time (s)			Memory	Time (s)			Memory
Length (m)	No. of Voxels	Empty	Con	Pol	Total	MByte	Con	Pol	Total	MByte	Con	Pol	Total	MByte
20	29x115x23	93.20%	12.04	0.16	12.21	10.17	12.84	0.19	13.02	9.78	14.58	0.18	14.76	11.07
15	39x157x30	94.32%	12.06	0.32	12.38	12.50	12.96	0.37	13.33	11.44	14.91	0.35	15.26	12.00
10	58x235x45	95.08%	12.07	0.8	12.87	20.09	12.95	0.96	13.92	16.19	14.92	0.91	15.82	16.69
5	116x476x89	96.38%	12.08	4.85	16.92	88.35	13.01	6.95	19.96	47.66	15.26	5.55	20.81	50.50
4	145x597x111	96.81%	12.24	9.21	21.45	158.94	13.08	12.83	25.91	76.70	15.58	10.61	26.19	80.31
3	194x800x148	97.42%	12.19	21.9	34.09	362.23	13.23	29.94	43.16	153.27	15.67	24.14	39.81	178.27
2	290x1199x222	98.21%	12.45	67.65	80.10	1153.13	13.69	95.85	109.54	389.34	16.16	75.29	91.45	417.98
1.5	387x1602x295	98.70%	12.83	151.48	164.31	2666.67	13.96	216.35	230.31	788.00	16.26	166.23	182.49	839.35
1	80x2405x443	99.24%	14.62	443.5	458.1	8556.78	15.43	672.07	687.5	1912.57	16.91	491.88	508.79	2056.805
			Integral Volumes				**Octree Max/Min**				**Integral Octree**			
Specifications			Time (s)			Memory	Time (s)			Memory	Time (s)			Memory
Length (m)	No. of Voxels	Empty	Con	Pol	Total	MByte	Con	Pol	Total	MByte	Con	Pol	Total	MByte
20	29x115x23	93.20%	12.9	0.15	13.05	10.38	14.65	0.21	14.86	18.32	15.67	0.23	15.9	18.27
15	39x157x30	94.32%	12.11	0.28	12.39	12.80	16.01	0.34	16.35	19.80	15.76	0.37	16.13	20.16
10	58x235x45	95.08%	12.17	0.68	12.85	20.43	16.12	0.89	17.01	25.68	16.32	0.92	17.24	25.93
5	116x476x89	96.38%	13.62	3.56	16.02	88.84	16.31	4.99	21.3	67.50	16.98	5.03	22.01	68.94
4	145x597x111	96.81%	13.32	6.48	19.81	159.08	16.62	9.45	26.07	110.24	17.45	9.67	27.12	117.25
3	194x800x148	97.42%	15.15	14.37	29.52	363.95	16.74	26.16	42.9	218.92	17.51	26.35	43.86	231.67
2	290x1199x222	98.21%	23.11	40.80	63.91	1154.02	17.21	63.02	80.23	595.01	18.14	64.08	82.22	720.01
1.5	387x1602x295	98.70%	39.64	86.54	126.18	2667.67	18.37	131.21	149.58	898.8	21.22	133.46	154.68	1068.43
1	80x2405x443	99.24%	111.38	210.94	322.32	8559.66	19.91	348.97	368.88	2087.71	25.83	352.31	378.14	2223.14

Table 6.7: Results: Execution time and memory consumption, Con=Construction, Pol= Polygonisation, MByte=Max Memory

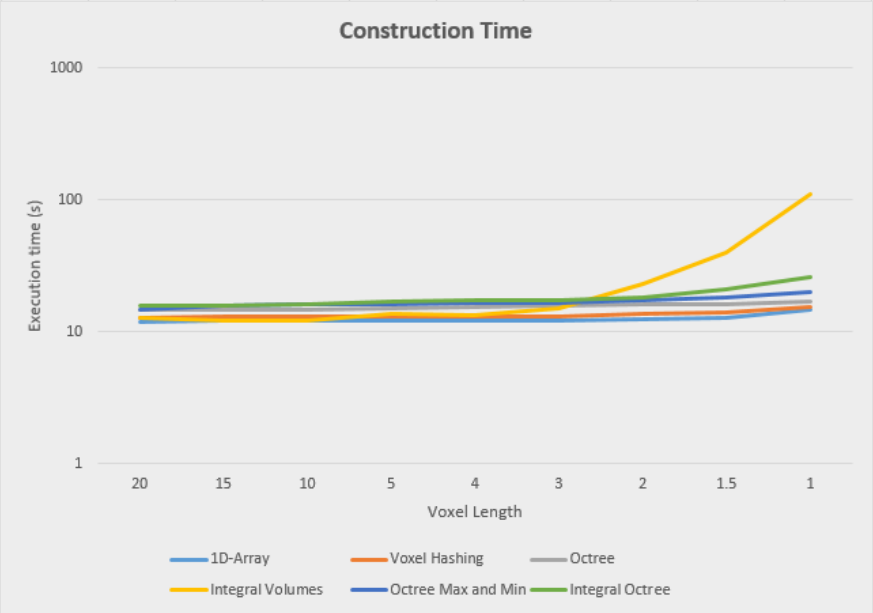

Figure 6-7: Time required to build each data structure by voxelising the FW LiDAR samples and inserting them inside the 3D volume (Table 6.7).

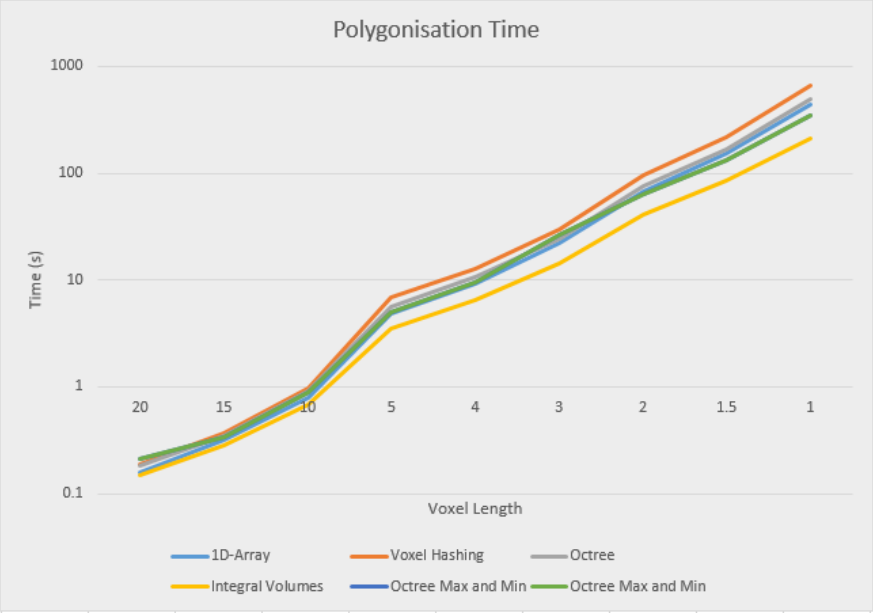

Figure 6-8: Time required to reconstruct the surface from the voxelised FW LiDAR data, after the data are voxelised (Table 6.7).

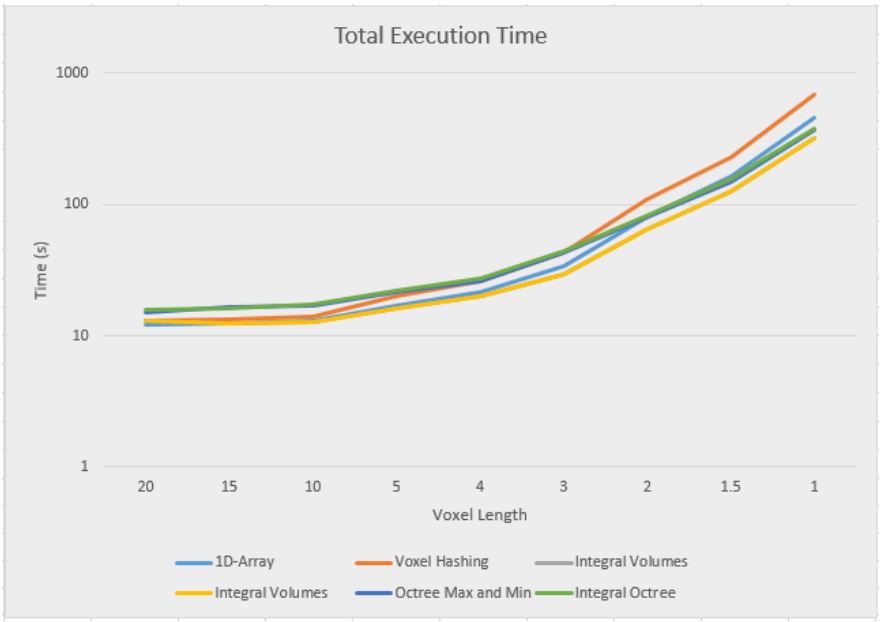

Figure 6-9: The sum of the time required to construct a data structure and the time required to generate a polygonal mesh (Table 6.7). The fastest one is the 'Integral Volumes'.

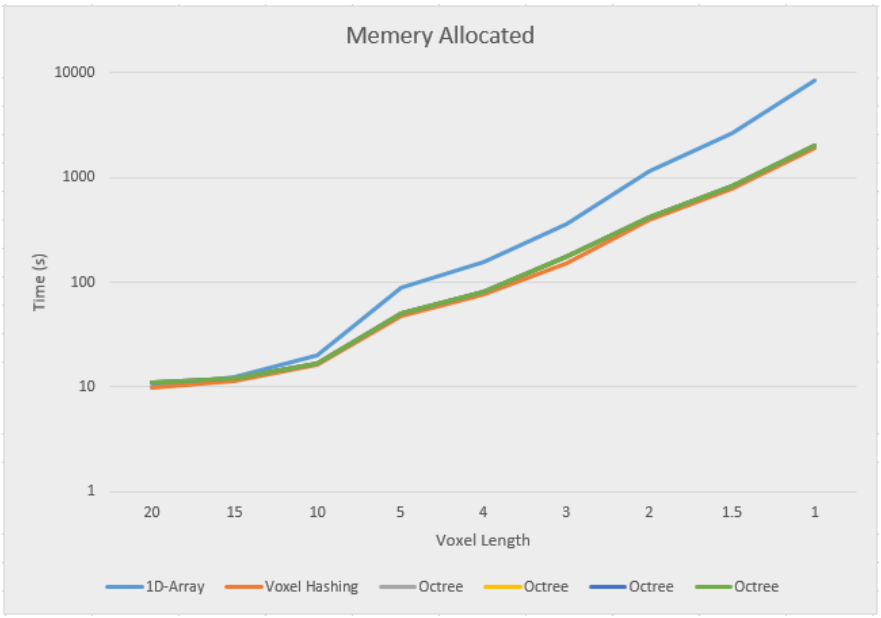

Figure 6-10: Maximum memory consumption at run time. '1D-Array' and 'Integral Volumes' consume the highest memory, which is approximately the same (Table 6.7).

			1D-Array				**Voxels Hashing**				**Octree**			
Specifications			Time (s)			Memory	Time (s)			Memory	Time (s)			Memory
Length (m)	No. of Voxels	Empty	Con	Pol	Total	MByte	Con	Pol	Total	MByte	Con	Pol	Total	MByte
6	96x250x76	97.34%	5.29	1.70	6.99	40.01	5.55	2.13	7.68	21.13	6.54	1.91	8.45	22.55
3	191x561x149	98.25%	5.38	11.73	17.11	237.39	5.67	16.76	22.43	80.45	6.71	13.18	19.89	83.95
1.5	381x1122x296	99.10%	5.82	85.51	91.33	1713.74	6.12	127.23	133.35	369.61	6.86	92.91	99.77	120.57
6	100x760x64	94.43%	22.21	4.38	26.59	84.55	23.65	6.40	30.05	48.10	31.04	5.07	36.11	52.23
3	199x1525x124	96.74%	22.48	38.57	61.05	608.29	24.05	51.31	75.36	281.26	30.9	42.70	73.6	292.18
1.5	398x3063x248	98.50%	69.42	159.5	228.92	4478.66	33.06	209.41	242.47	1553.92	32.05	226.85	258.9	1596.43
6	382x90x108	96.60%	22.43	2.75	25.18	62.50	24.45	3.87	28.32	29.67	32.58	3.19	35.77	32.16
3	763x178x213	97.52%	21.95	18.20	40.15	397.73	23.81	28.42	52.23	126.06	32.05	21.20	53.25	37.37
1.5	1526x355x424	98.38%	22.84	164.73	187.57	3044.09	25.03	261.64	286.67	707.75	33.00	169.8	202.8	769.43
			Integral Volumes				**Octree Max/Min**				**Integral Octree**			
Specifications			Time (s)			Memory	Time (s)			Memory	Time (s)			Memory
Length (m)	No. of Voxels	Empty	Con	Pol	Total	MByte	Con	Pol	Total	MByte	Con	Pol	Total	MByte
6	96x250x76	97.34%	5.50	1.23	6.73	40.05	9.40	1.67	11.07	31.50	7.17	2.07	9.24	30.88
3	191x561x149	98.25%	7.13	6.80	13.93	237.75	7.51	10.89	18.40	111.52	7.06	11.33	18.39	105.68
1.5	381x1122x296	99.10%	23.98	40.13	64.11	1714.71	8.49	62.73	71.22	443.09	8.34	63.60	71.94	417.36
6	100x760x64	94.43%	22.69	3.19	25.88	89.9	32.26	5.17	37.43	82.86	32.70	6.70	39.40	68.93
3	199x1525x124	96.74%	28.04	26.86	54.90	608.79	32.43	32.70	65.13	176.47	31.94	46.50	78.44	396.45
1.5	398x3063x248	98.50%	69.42	159.50	228.92	4478.66	33.06	209.41	242.47	653.92	32.05	226.85	258.9	1546.43
6	382x90x108	96.60%	23.12	1.80	24.92	63.02	33.76	2.77	36.53	45.84	34.56	2.62	37.18	40.33
3	763x178x213	97.52%	24.53	9.87	34.40	398.16	33.43	14.92	48.35	183.02	34.63	12.96	47.59	187.89
1.5	1526x355x424	98.38%	62.25	99.75	162.00	3045.41	33.54	134.56	168.10	934.25	33.96	135.79	169.75	1064.62

Table 6.8: Execution time and memory consumption results from 3 different flightlines.

	Empty Voxels (Percentage)	Construction Time (Seconds)	Polygonisation Time (Seconds)	Total Time(Seconds)	Maximum Memory (MBytes)
1	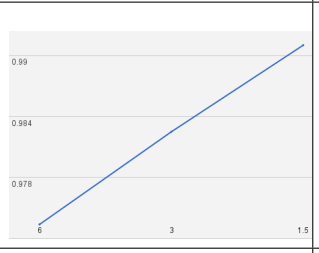	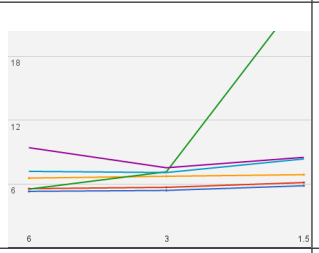	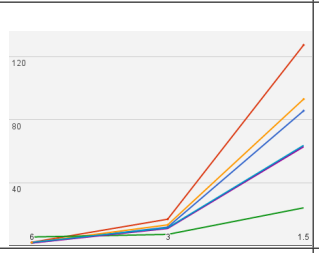	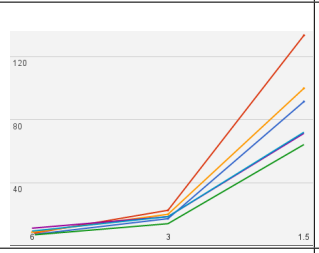	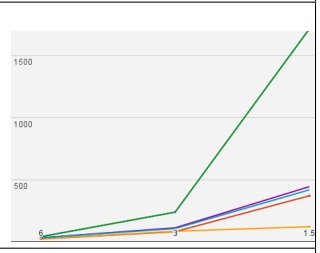
2	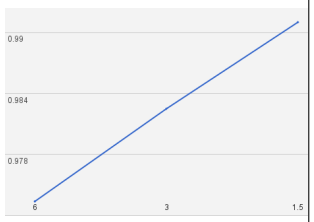	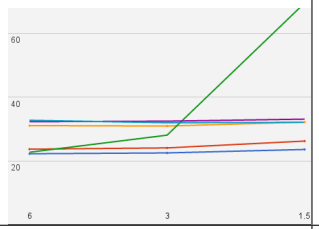	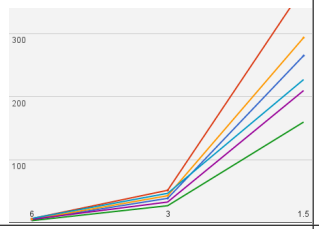	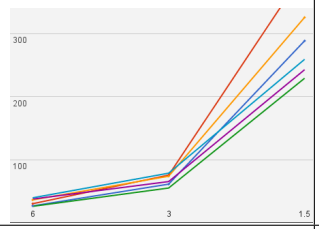	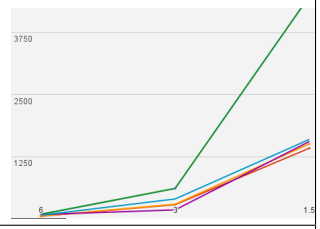
3	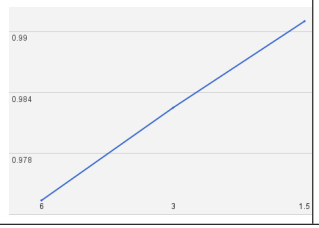	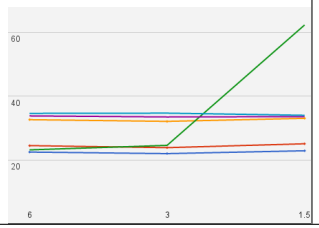	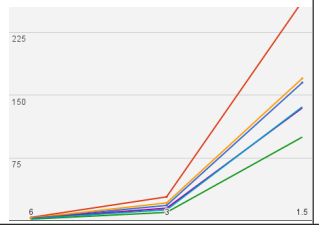	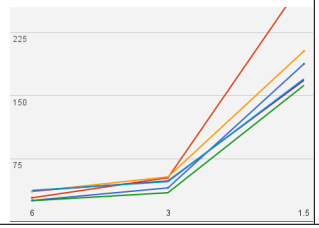	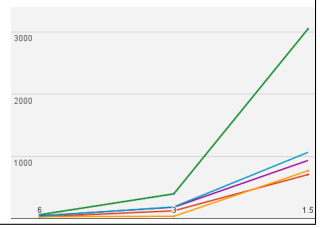

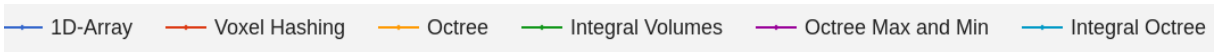

Table 6.9: Chart diagrams generated using the results from Table 6.8. The 1st flightline is from the New Forest Dataset (LDR-FW-FW10_01-201009822.LAS). The 2nd flightline is from the Dennys Wood dataset (LDR-FW10_01-201018713.LAS) and the 3rd one from Eaves Wood (LDR-FW-GB12_04-2014-083-13.LAS).

6.9 Discussion

Overall, 'Integral Volumes', the main new approach proposed, is the fastest one but it consumes as much memory as the original '1D-Array'. It's performance is better than the 'Octree Max and Min' because:

- Elements are accessed in constant time while traversing a tree requires at least O(log n) time, when the tree is balanced, and up to O(n) for unbalanced trees.
- The size of the volume is the original cuboid while any octree data structure requires a cubic space that is a power of two. This results into extending the boundaries of the 3D voxelised FW LiDAR, including big empty areas and building deeper and unbalanced trees (increased traversal time).
- Neighbours finding is faster than octrees since no backtracking is required.
- Checking whether a surface is crossing the edges of an empty area is much faster using the 'Integral Volumes' because the sum of any volume is calculated in constant time. Therefore checking whether the neighbours are empty as well is trivial. While for the 'Octree Max/Min' and 'Integral Tree' data structures, it's required to loop through all the voxels at the edges of an empty branch to avoid generating holes.

Regarding the 'Voxel Hashing', faster results were expected than the 'Octree' because it doesn't required traversal for reaching elements, but it's very likely to have more jumps in memory, considering that the implementation of the octree structures, keeps the children of every branch coherent in memory for faster interpretation.

Furthermore, 'Octree Max and Min' and the 'Integral Octree' have similar results. In the tests, the isolevel was set lower than the noise threshold and for that reason the empty branches were the ones discarded at the tests (Line 6 of Algorithm 3). If the isolevel was lower than the noise threshold, then the low level noise would have affected the 'Octree Max and Min' less than the 'Integral Octree'; the 'Octree Max and Min' check whether the max value is below the threshold, while the 'Integral Octree' the sum of the leaves. Additionally, 'Integral Octree' consumes more memory for saving the leaves into an 1D-array, but even though 'Integral Ocree' generally performed worse than the 'Octree Max/Min' in the tests of Table 6.7 and 6.8, it should be beneficial in multi-resolution direct volumetric rendering and blurring the volume for noise removal.

To sum up, 'Integral Volumes' is a new and simple algorithm presented in this thesis and it is the fastest one for the surface reconstruction of voxelised FW LiDAR in comparison to 'Voxel Hasing' and octrees.

Chapter 7

Alignment with Hyperspectral Imagery

7.1 Introduction

In this chapter, the hyperspectral images are introduced to improve the visual output of the polygonal meshes derived from the FW LiDAR data (Chapter 5). The combination of NERC-ARF LiDAR and hyperspectal data from New Forest (Figure 2-1) for generating tree coverage maps is investigated.

Please note that definitions (i.e. bands and level-1) are used in this chapter and if you are not familiar with these terms it is highly recommended to read again Section 2.4, which explains everything about hyperspectral imagery.

7.2 Previous Work

Regarding the integration of FW LiDAR and hyperspectral data in remote forest surveying, there are diverse opinions on whether the integration of multi-sensor data improves remote forest surveying. Clark et al. attempted to estimate forest biomass but no better results were observed after the integration [34], while the outcomes of Anderson et al. for observing tree species abundances structures were improved after the integration of the data [35].

Buddenbaum et al. [36], and Heinzel and Koch [37], used a combination of multi-sensor data for tree classifications. Buddenbaum et al. use fusion of data to generate RGB images from a combination of FW LiDAR and hyperspectral features, although the fusion reduces the dimensionality of a classifier [36]. In that study, three different classifiers were implemented and the Support Vector Machines (SVMs) returned the

best results. SVMs were also used in [37] to handle the high dimensionality of the metrics (464 metrics). In that research a combination of FW LiDAR, discrete LiDAR, hyperspectral and colour infrared (CIR) images are used. Each of the 125 hyperspectral bands was directly used as a feature in the classifier, contributing to the high dimensionality.

7.3 Spatial Representation of Hyperspectral Pixels for Quick Search

For the New Forest Dataset (Figure 2-1), there are both FW LiDAR and hyperspectral data. The data are collected from two independent instruments and, while they are flown together, each instrument has a slightly different view point, a different resolution/sensing mechanism and data collection parameters (e.g. integration time). Therefore the data collected are not aligned to each other (e.g. for each waveform there is no trivial-correspondence to a spectral measurement). To integrate the data geo-spatially, alignment of the data is required. As mentioned at Section 2.4, in order to preserve the highest possible quality and reduce blurring that occurs during geo-rectification, data in the original sensing geometry (level-1) are used.

In Anderson et al. [35], an inverse distance weighted algorithm is used to rasterise the hyperspectral images and the pixel size is constant, 15.8m, while in this study an approach similar to Warren et al. [13] is used and the resolution is changeable. The main concept of our geo-rectification algorithm is to be able to find the nearest hyperspectral pixel to a point in the fastest possible way. For that reason, a spatial representation of the hyperspectral pixels is created by importing the pixels into a 2D grid, similar to [13]. The cell size of the grid in meters is constant, but the dimensions of the grid in number of squares (n_x, n_y) can be varied according to the chosen average number of pixels per square (A_{ps}):

$$n_x = \sqrt{\frac{n_s^2}{A_{ps}}} \qquad n_y = \sqrt{\frac{n_l^2}{A_{ps}}} \tag{7.1}$$

Where n_s is the number of samples and n_l is the number of lines of the hyperspectral cube (figure 2-4).

Furthermore, Warren et al. [13] uses a tree-like structure, here a structure similar to hash tables is used to spatially represent the pixels and speeding up searching. As shown in Figure 7-1, for each cell there is a bucket containing all the points that lie inside it. The hash function takes as input the unique key of the cell and returns the

memory location of the corresponding bucket. The key of a cell with coordinates (x_s, y_s) is is equal to $(x_s + y_s * n_x)$ where n_x is the number of pixels in the x-axis.

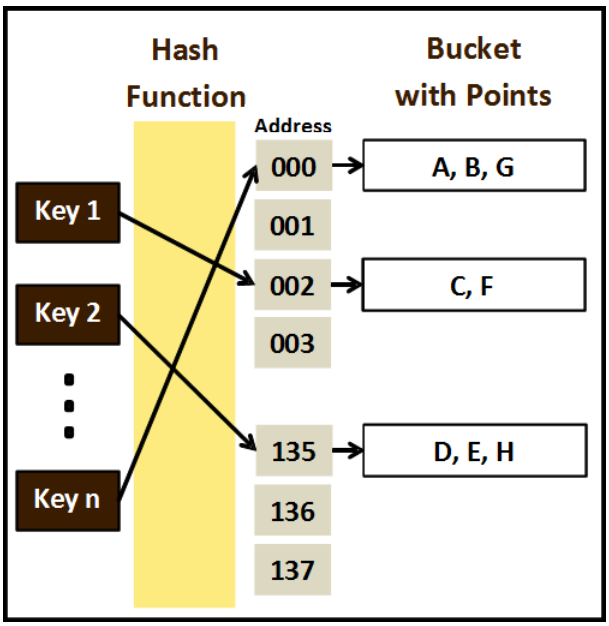

Figure 7-1: The hash table of the spatial representation of the hyperspectral pixels; each bucket contains all the pixels in a square and has a unique key derived from the coordinates of its square. The hash function takes as input the key and returns the address in memory of the corresponding bucket.

The next step is for a point (x_v, y_v, z_v) to find the pixel whose geolocation is the closest to it. First we project the point into 2D by dropping the z coordinate and then we find the square (x_s, y_s) that the projected point $\mathbf{v}(x_v, y_v)$ lies inside, as follow:

$$x_s = \frac{x_v - X_{min}}{X_{max} - X_{min}} * n_x \tag{7.2}$$

$$x_s = \frac{y_v - Y_{min}}{Y_{max} - Y_{min}} * n_y \tag{7.3}$$

Where X_{max}, X_{min}, Y_{max}, Y_{min} are the geospatial boundaries of all the hyperspectral image and n_x, n_x are the number of pixels in the x and y axis accordingly.

From the square (x_s, y_s) we can get the set of pixels that lie inside the same square with the point of our interest. Let's assume that the geospatial locations of these pixels are the vectors $\mathbf{g_1}, \mathbf{g_2}, \mathbf{g_3}, ..., \mathbf{g_n}$ respectively. Then, by looping through that set of pixels, we can find the pixel i that is most likely to be the closest pixel to the point

$\mathbf{v}(x_v, y_v)$:

$$i = \arg\min |\mathbf{v} - \mathbf{g_i}|^2. \tag{7.4}$$

Finally, there is the case of the closest point to be within an adjacent square and this occurs when the point is very close to the edges of the square. Even though this was not implemented in DASOS when the paper [24] was published, it can be done by checking the distance between the edges of the square and the point. If this distance is smaller than the distance between pixel i then we can loop through the points of the corresponding adjacent square and check whether there is another pixel closer to point $\mathbf{v}$ than pixel i. Similarly, by checking the distance between the point $\mathbf{v}$ and the corners of the square (x_s, y_s), the case of the closest point to exist inside a diagonally-adjacent square is also covered.

7.4 Projecting hyperspectral images into polygon meshes generated using FW LiDAR data

This section focuses on projecting the (level-1) hyperspectral images onto the polygonal meshes reconstructed from the FW LiDAR data as explained in Section **??**. As shown in Figure 7-2, the result is a coloured polygon mesh. That mesh is saved into two files:

- the .obj file that contains the 3D geometry and
- the .png file that contains the 2D texture image

The (level-1) hyperspectral images look deformed because the pixel size is not consistent. (Figure 7-2 shows that inconsistency). DASOS resolves this problem by adjusting the texture coordinates of the polygonal mesh according to the geolocation of the pixels. The texture coordinates (u, v) of each vertex lies inside the range $[0, 1]$ and if they are multiplied by the height/width of the texture, then the position of the corresponding pixel of the texture is given. In order to calculate the texture coordinates of each vertex (x_v, y_v, z_v), the spatial representation of the hyperspectral pixels (explained at Section 7.3) is used for quickly detecting the pixel (x_p, y_p), whose geolocation is the closest to a vertex. By dividing the pixel position with the number of samples (n_s) and lines (n_l) in the hyperspectral image, the texture coordinates (u, v) of each vertex $v(x_v, y_v)$ are calculated:

$$u = \frac{x_p}{n_s} \qquad v = \frac{y_p}{n_l} \tag{7.5}$$

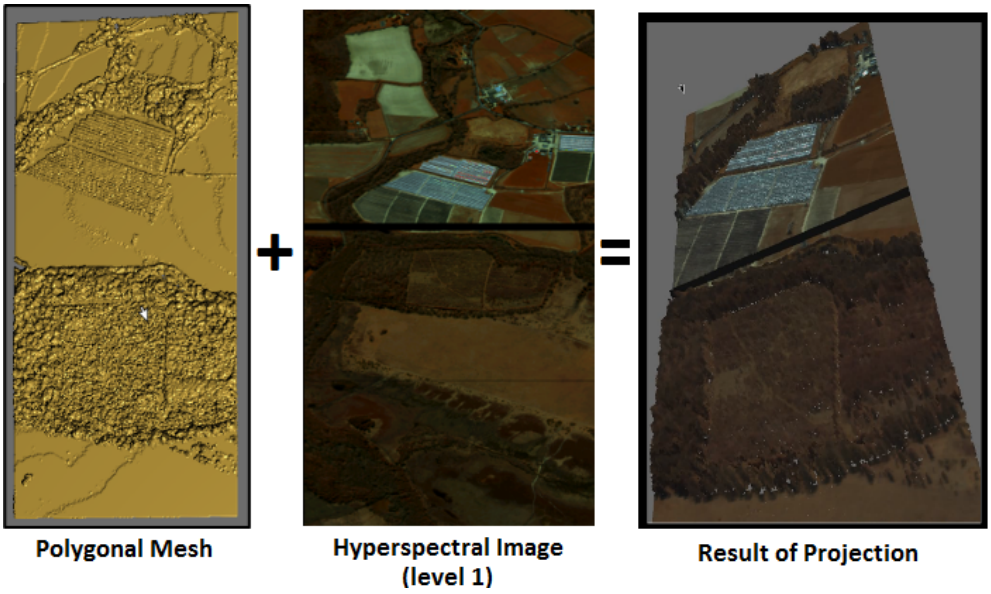

Figure 7-2: Projecting hyperspectral images into the polygonal meshes

Regarding the outputs, the texture coordinates of the polygonal mesh are added into the .obj file, while the 2D texture is simply an image generated from three user-selected bands for the RGB colours. The width of the image is equal to the number of hyperspectral samples per line while its height is equal to the number of lines.

7.4.1 Results

The results of the projection are coloured polygonal meshes. Each coloured polygonal mesh is exported into two files:

1. the .obj file contains the 3D geometry with all the information about the vertices, edges, faces, normals and texture coordinates, and

2. the .png is the 2D texture (an RGB image) and it is aligned with the texture coordinates of the polygonal mesh.

Figure 7-3 shows how the visual output is affected by projecting hyperspectral data from different sensors and by changing the selected bands.

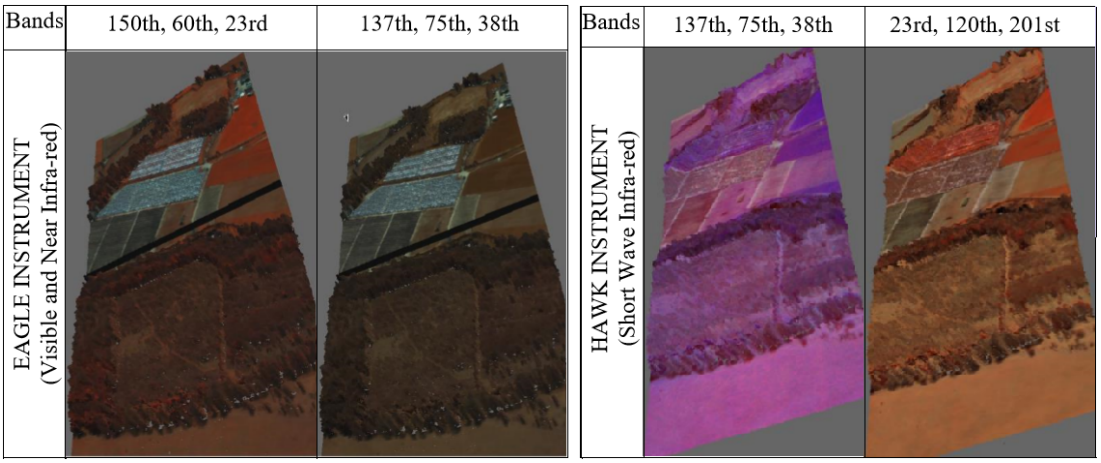

Figure 7-3: Results of Alignment; the left table shows the results of projecting hyperspectral images from the Eagle instrument onto the polygonal meshes generated using FW LiDAR data and the right hand side table shows results using the Hawk instrument.

7.5 Tree Coverage Maps

As mentioned before, there are diverse opinions on whether or not integration of remotely sensed data improves forest monitoring [34] [35]. For that reason, a simple pixelwise classifier was implemented to test how the integration of NERC-ARF data, using metrics generated from DASOS, performs for generating tree coverage maps.

The metrics generated from both hyperspectral and FW LiDAR data are 2D aligned images (Table **??**). In other words, the pixel (x, y) has the same geospatial coordinates in every metric. Further the resolution of the metrics depends on the resolution of the 3D voxelised FW LiDAR data (Section **??**). If the dimensions of the volume are (x, y, z) then the dimensions of the metrics are (x, y). For the LiDAR metrics, each pixel is coloured according to the information derived from the corresponding column. Regarding the hyperspectral metrics, (level-1) data are used to preserve the highest possible quality. The method in Section 7.3 was used for finding the pixel from the hyperspectral data with the closest geospatial location to the centre of each column of the 3D voxelised FW LiDAR.

The metrics used for generating tree coverage maps are grouped into two categories (FW LiDAR and hyperspectral metrics):

- FW LiDAR: Height (L0), Thickness (L1), Density (L2) and First Patch (L3)
- Hyperspectral: Mean (H0), NDVI (H1), Standard Deviation (H2) and Spectral Signature (H3)

For more descriptive information and examples of the metrics please look at Table **??**,

where all the functionalities of DASOS are listed.

7.5.1 Testing and Results

In this case, the total accuracy was increased with the integration of FW LiDAR data and hyperspectral images. A Naïve Bayesian classifier using a multi-variance Gaussian model is applied for distinguishing tree-covered areas from the ground. The main idea is for each pixel/column to find the class that is more likely to belong to Tree or Ground. Ground truth data were hand painted using 3D models generated with DASOS and were divided into training and testing data. There are three test cases and, for each test case, the following metrics are used:

- 1st test case uses the L0-L3 metrics that are generated from the FW LiDAR data.
- 2nd test case uses the H0-H3 metrics that are generated from the hyperspectral imagery.
- 3rd test case uses L0-L3 & H0-H3 which is a combination of metrics generated from either FW LiDAR data or hyperspectral imagery.

For each test case, an error matrix is generated to indicate the accuracy of the classification results as verified against the ground truth data (Tables 7.1, 7.2 and 7.3) [38]. Each row shows the number of pixels assigned to each class relative to their actual class. For example, the first row of Table 7.1 shows that 130445 pixels were classified as trees, where 125375 were actual trees and the rest 5070 were ground. From the error matrices, the classification accuracy of each test case was calculated and it is presented in Table 7.4.

Figure 7-4 depicts the coverage maps generated for each test case. Three areas are marked for comparison. In Area 1 there is low vegetation, in Area 2 there are short trees and in Area 3 warehouses. Area 1 was incorrectly classified when only the hyperspectral data were used; when the height information of the LiDAR data was included into the classifier, area 1 was correctly classified. Similarly, Area 2 was wrongly classified when using the only FW LiDAR metrics because the height of the trees was less than the average training samples. But since features from the hyperspectral data are not height dependant, the classification results of test case 1 (with hyperspectral metrics) was better at Area 2. Area 3 seems to confuse the first two classifiers in different ways, but the combination improved the results.

Finally, to demonstrate the usefulness of DASOS's polygonal meshes, the results of the tree coverage maps were projected into the polygon representations as shown in the following Figure 7-5.

		Ground truth data		
		Tree	Ground	Row Total
Results	Tree	125375	5070	130445
	Ground	45093	228495	273588
	Total	170468	233565	404033

Table 7.1: Error Matrix showing the pixel-wise classification results of the 1st test case that only uses hyperspectral data.

		Ground truth data		
		Tree	Ground	Row Total
Results	Tree	154768	39504	194272
	Ground	15700	194061	209761
	Total	170468	233565	404033

Table 7.2: Error Matrix showing the pixel-wise classification results of the 2nd test case that only uses FW LiDAR data.

		Ground truth data		
		Tree	Ground	Row Total
Results	Tree	152597	10548	163145
	Ground	17871	223017	240888
	Total	170468	233565	404033

Table 7.3: Error Matrix showing the pixel-wise classification results of the 3rd test case that uses both hyperspectral and FW LiDAR data.

	FW LiDAR	**Hyperspectral Imagery**	**Both**
Tree	73.55%	90.79%	89.52%
Ground	97.83%	83.09%	95.48%
Mean Average Precision	87.58%	86.34%	92.97%

Table 7.4: Classification accuracy of each test case

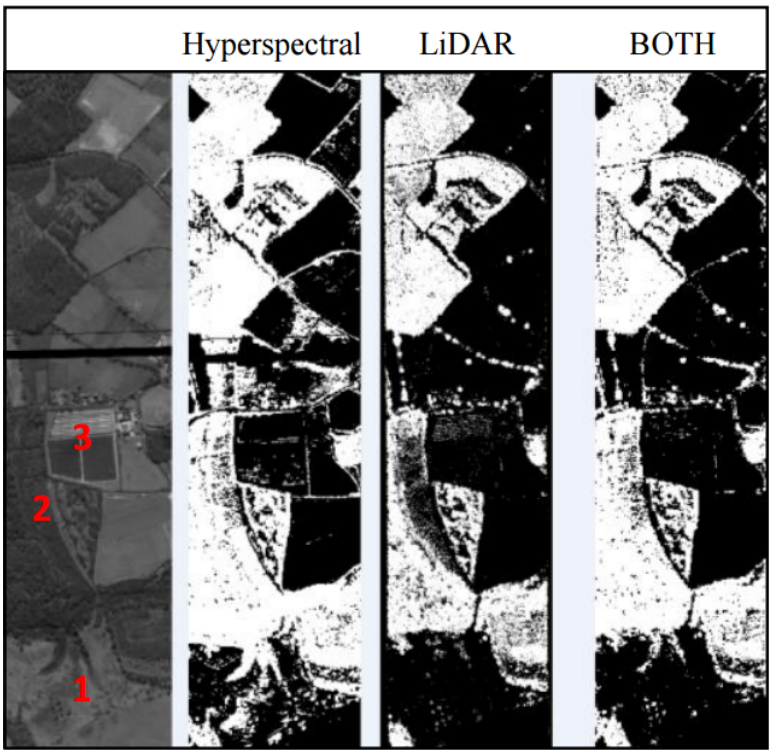

Figure 7-4: Visual Comparison of the results of the coverage maps

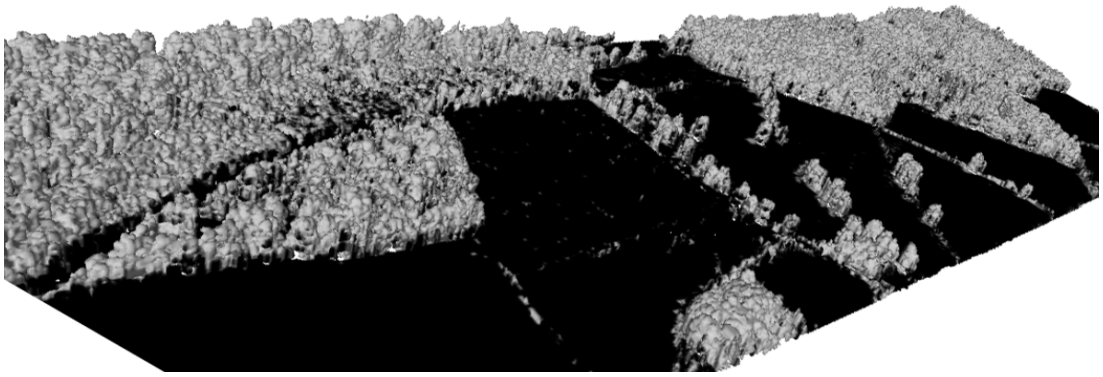

Figure 7-5: 3D Coverage model, generated by projecting the results of the tree coverage classification into a polygonal mesh.

7.6 Summary and Conclusions

In conclusion, this chapter describes an efficient way of aligning the FW LiDAR data and hyperspectral images using a spatial representation of hyperspectral pixels. The voxelisation of the FW LiDAR data also eases the generation of aligned metrics from both datasets. Furthermore, the resolution of the metrics is changeable and depends on the user-defined resolution of the voxelised FW LiDAR data. Additionally, since the closest pixel is always selected, regardless of the distance from the point of interest, the problem of having data at different resolution is automatically resolved.

Regarding the results, coloured polygonal meshes were generated using the alignment and the result demonstrated that the integration of this specific data has potential in remote forest surveying - aside from improving the visual appeal, it also improves automatic classification. This was shown using a simple classifier for generating tree coverage maps. The results were positive; the classification accuracy was improved by 5.39% when both datasets were used. A more sophisticated classifier would likely give even better results.

Chapter 8

Detection of Dead Standing Eucalyptus For Managing Biodiversity in Native Australian Forest

8.1 Introduction

8.1.1 The Importance of Dead Wood

The value of dead trees from a biodiversity management perspective is large. Once a tree dies, its contribution to our ecosystem continues. The woody structure remains for centuries and it contributes to forest regeneration while providing resources for numerous surrounding organisms [39]. As an indication, more than 4000 species inhabit dead wood in Finland [40], where an estimate of 1000 species has been extinct [41]. These species do not only include animals and birds but also organisms, like fungi. Fungi contributes to wood decaying, formation of hollows and biodiversity, which is an important factor for a resilient ecosystem [42]. Observing the changes of fungal diversity on decaying wood has an increased interest in science [43] [44] [45] in order to ensure the continuous existence of decaying wood in forests.

** NEill comma where: Specifically, in Australia, tree

Specifically in Australia, tree hollows play a significant role in managing biodiversity. Nearly all arboreal mammals rely on hollows with the exception of the Koala and perhaps Ringtail Possums that preferentially make a stick nest, but they use hollows as well. Additionally, a large number of Australian bird species rely on hollows for shelters

[46]. Nevertheless, Australia has no real hollow creators unlike the northern hemisphere (e.g. Woodpeckers), and therefore it relies predominantly on natural processes of limb breakage, insect and fungal attack when access points are provided through damage caused by wind, storms and fire.

This kind of hollows take hundreds of years to form and because of that it is more likely to exist on dead trees. In Australia, studies predict shortage of hollows for colonisation in the near future [47] [48]. Therefore automated detection of them plays a significant role in protecting those animals. As an indicator of the importance of hollows in managing biodiversity, a list of a few of the species that rely on hollows was provided by the Forestry Corporation of NSW. Those species are shown at Figure 8-1. According to the Department of the Environment of Australian Government and the Government of Western Australia, six of them are protected, threatened or close to extinct [49] [50]. Figure 8-1 shows the species from the provided list and the six protected species have a red border and their names are bold in the description.

For the aforementioned reasons, monitoring dead trees is essential for having a resilient ecosystem. Nevertheless, the distribution of dead trees significantly varies making detection of them difficult [51]. Remote sensing approaches has been introduce to automate the process of monitoring forest and further increase the spatial resolution of the monitored area. The following section gives an overview of the related work undertaken in Remote Sensing.

8.1.2 Related Work

Remote Sensing was introduced for automatically detecting dead trees, because field-work is time consuming considering their variance spread and the size of the relevant forests. From a classification perceptive, the task of identifying dead standing and dead fallen trees is different. Fallen trees are identified by detecting segments or line-like features on the terrain surface using LiDAR data [52] [53]. Regarding standing dead trees, their shape (reduced number of leaves or broken branches) [54] and light reflectance (less green light illuminated) [55] are important factors for identifying them.

Previous work on dead standing trees detection performs single tree crown delineation before health assessment [54] [56]. Tree-crown delineation is usually done by detecting local maxima from the canopy height model (CHM) and then segmenting trees with watershed algorithm [57]. Improvements has been achieved by introducing markers controlled watershed [58] and structural elements of tree crowns with different sizes [59]. Additionally, Popescu and Zhao analyse the vertical distribution of the LiDAR points in conjunction with the local maximum filtering of CHM [60].

In the case of Eucalyptus, single tree detection is a challenge on its own, due to their

Figure 8-1: A number of species that rely on tree hollows of which the red ones / bold ones are close to extinction: Kookaburra, Sulphur Crested Cockatoo, **Corella**, Crimson Rosella, Eastern Rosella, Galah, Rainbow Lorikeet, Musk Lorikeet, Little Lorikeet , Red-winged Parrot, **Superb Parrot**, Cockatiel, Australian Ringneck (Parrot), Red-rumped Parrot, Powerful Owl, Sooty Ow, Barking Owl, **Masked Owl**, **Barn Owl**, White-throated Treecreeper, Hollow Owl, **Brush-tailed Possum** (mammal) [1]

[1]The images of the birds were taken from the following links (Retrieved on the 27th of April 2016): Kookaburra: <http://tenrandomfacts.com/blue-winged-kookaburra/>, Sulphur Crested Cockatoo: <http://aussiegal7.deviantart.com/art/Sulphur-Crested-Cockatoo-08-153341893>, Corella: <http://www.theparrotplace.co.nz/all-about-parrots/long-billed-corella/, Superb Parrot: <http://www.davidkphotography.com/?showimage=637>, Crimson Rosella: <http://25.media.tumblr.com/tumblr_m3mo89c40r1r4t9h1o1_1280.jpg>, Eastern Rosella: <http://2.bp.blogspot.com/-pYxw51WjSOY/UB-LEFgd2KI/AAAAAAAAAWg/9z60PUWE6TE/s1600/_GJS6601-as-Smart-Object-1.jpg>, Rainbow Lorikeet: <https://www.reddit.com/r/pics/comments/328fvc/a_rainbow_lorikeet_found_in_coastal_regions/>, Musk Lorikeet: <http://www.rymich.com/girraween/photos/animals/birds/medium/glossopsitta_concinna/glossopsitta_concinna_001.jpg>, Little Lorikeet: <http://www.pbase.com/sjmurray/psittacidae>, Red-winged Parrot: <https://www.pinterest.com/pin/395894623469889727/>, Cockatiel: <http://up.parsipet.ir/uploads/Cockatiels-for-sale.jpg>, Australian Ringneck (Parrot): <http://ontheroadmagazine.com.au/wp-content/uploads/2015/09/Twenty-eight-parrot-2-min.jpg>, Red-rumped Parrot: <http://parrotfacts.net/wp-content/uploads/Red-Rumped-Parrot-on-a-tree.jpg>, Powerful Owl: <http://farm1.staticflickr.com/219/495796536_f78dac04c1.jpg>, Sooty Owl: <ttp://www.mariewinn.com/marieblog/uploaded_images/screech2-738532.jpg, Barking Owl: <http://www.pcpimages.com/Nature-and-Wildlife/Birds/i-7JKSTp5/1/L/owl%20%281%20of%201%29-L.jpg>, Masked Owl: <http://www.survival.org.au/images/birds/masked_owl_2_600.jpg>, Galah: https://www.pinterest.com/pin/537546905498955709/>, White-throated Treecreeper: <https://geoffpark.files.wordpress.com/2011/09/female-white-throated-treecreeper.jpg>,

irregular structure and multiple trunk splits. In other words, each tree trunks splits create a local maximum leading into over-segmentation when tree crowns are detected by local maxima filtering. Shendryk published a eucalyptus delineation algorithm that starts segmentation from bottom to top. In this paper, the trunks point cloud is separated from the leaves and individual trunks are identified before proceeding to crown segmentation [61]. Nevertheless, for that project only 17 flightlines of LiDAR data were collected. The density resolution starts from 12 points/m^2 and goes up to 36 points/m^2 around forested areas. For small research projects capturing this high resolution is acceptable, but for commercial use and larger areas, the density of data collected is above the optimal resolution for a cost effective versus quality acquisition [62]. The project of this thesis is much larger. The resolution of our acquired LiDAR data has an average of four pulses per square meter,which is considered an optimal resolution in relation to the cost. But because of the tree height (up to 43m according to the fieldwork), a small amount of pulse intensity reached the trunks and the recordered waveform do not include enough information for individual trunk detection. An example of this project's discrete LiDAR data is shown in Figure 8-2 and the missing information about the trunks is depicted.

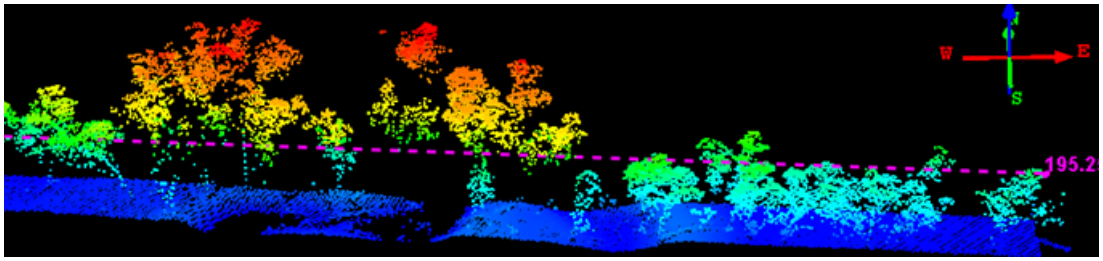

Figure 8-2: LiDAR point cloud showing that there are very limited points reflected from tree trunks.

***Note read again to make sure it matches OK

The acquired data are full-waveform LiDAR data. Traditional ways of interpreting FW LiDAR data, suggests extraction of a denser points cloud using Gaussian decomposition [15] [16]. Nevertheless, in this project we uses the open source software DASOS. DASOS was influenced by Persson et al, 2005, who used voxelisation to visualise the waveforms [20]. But, it does not only uses voxelisation for visualisations but also for extracting metrics useful in classification. It further normalises the intensities so that equal pulse length exists inside each voxel, making intensities more meaningful. It is further seems that the literature is moving towards voxelisation with promising results obtained at recent publication on tree species classification [21].

Hollow Owl: <http://www.mariewinn.com/marieblog/uploaded_images/screech2-738532.jpg>

Here, it is introduced an approach for quick dead tree detection derived from the boost cascade approach [63] but extended into 3D. This approach further contains similarities of the 3D tree shape signatures proposed by Dong, 2009, for distinguishing Oaks from Douglas fir tree crowns [64].

8.2 Materials

In this section, information about the study area, the acquired remote sensing and field data are provided. Figure 8-3 depicts all of them on a map, while section 8.2.1, 8.2.2 and 8.2.3 give technical information about them.

*** NEIL: What information?

8.2.1 Study Area

The study area is a native River Red Gum (Eucalyptus camaldulensis) forest of size $542km^2$ in south-eastern Australia. The regeneration of the eucalyptus is extremely dependant in floods and therefore, their distribution in respect to density, health and age is highly variance [65]. Additionally, the height of Eucalyptus camaldulensis reaches up to $30 - 40m$ and their structural complexity is high with multiple trunk splits [66]. The size and structure of the forest, with a human as reference, is depicted in Figure 8-4, while examples of the variance shape of dead trees is shown in Figure 8-5.

8.2.2 Acquired full-waveform LiDAR data

Multiple-echo, full-waveform (FW) LiDAR data are supplied by RPS Australia East Pty Ltd. The data were acquired from 900m above ground level, using the Trimble AX60 Airborne LiDAR sensor, which was released in October 2013 [67]. The wavelength of the emitted laser was 1062nm, the maximum scan angle was 60 degrees, and the pulse rate was 400kHz. The acquisition was held from the 6th of March till the 31st of March 2015. The collected LiDAR were delivered into 206 flightlines, of which 13 are cross runs used for geometric correction. There is also a 30% of swath overlap. The point spacing along and across the track is 0.48m and the average point spacing is 4.3 points per square meter. Figure 8-6 shows an example of a dead tree in respect to the acquired discrete LiDAR point cloud. Detailed information about FW LiDAR related concepts are given in section 2.

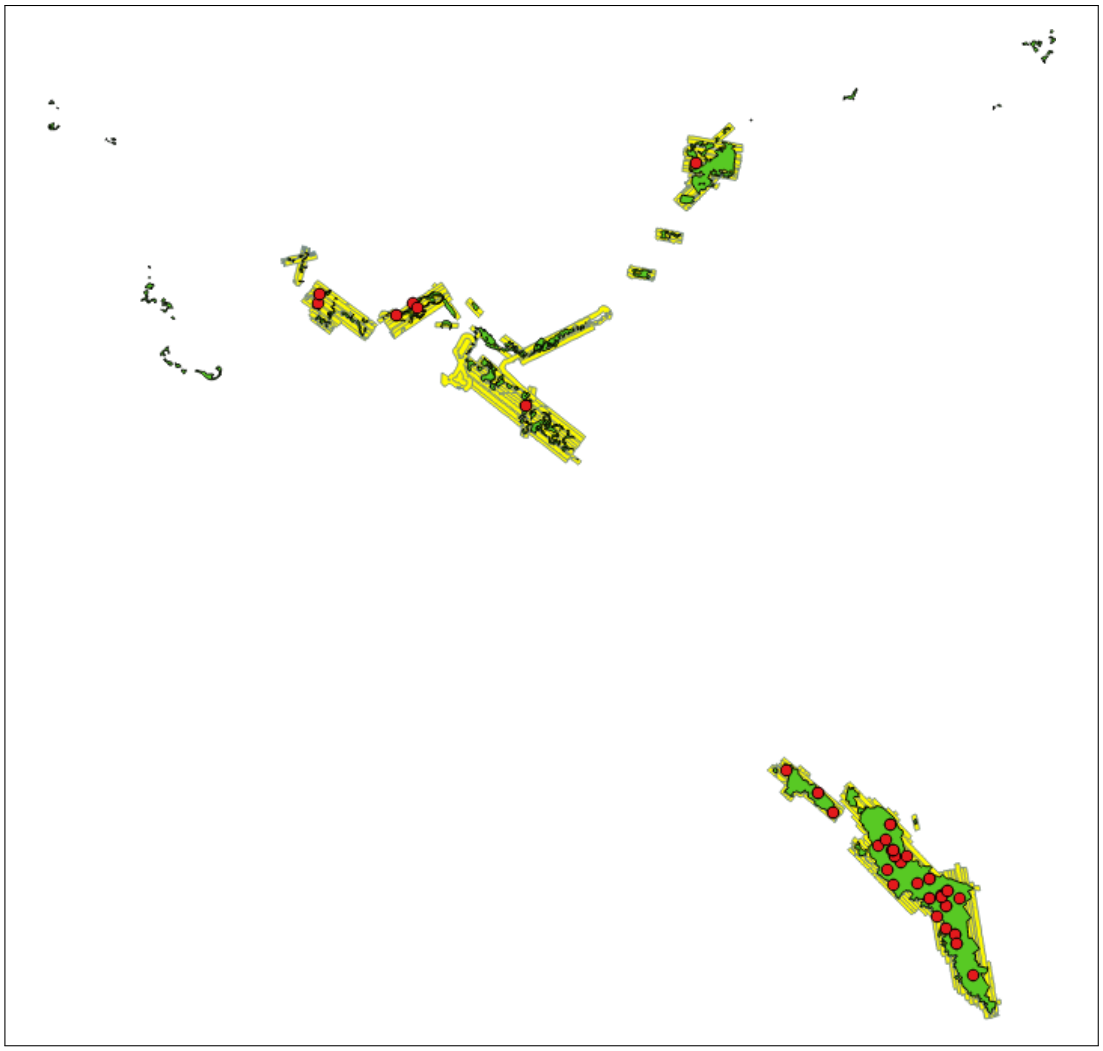

Figure 8-3: The study area is depicted by green ($542km^2$), the yellow strips are the LiDAR flightlines and the red dots are the position of the field plots.**Note: this image many need to be removed due to confidentiality of the company. I will talk with them and hopefully it will be ok.

8.2.3 Field Data

The field data were collected in July 2015 during the winter season of Australia and they include tree and canopy related measurements on circular plots. There are 33 plots with radius 35.68m and area 0.4ha allocated randomly inside the study area. On these plots, a total of 2386 trees were individually measured. Tree measurements include the geo-location, the trunk diameter at the standard height of 1.3m (breast heigh), height, species and health conditions (i.e. dead or alive). The geo-location of each tree is defined

Figure 8-4: Structure of Red Gum Forest in south-eastern Australia.

Figure 8-5: Example of dead trees indicating their variance in shape.

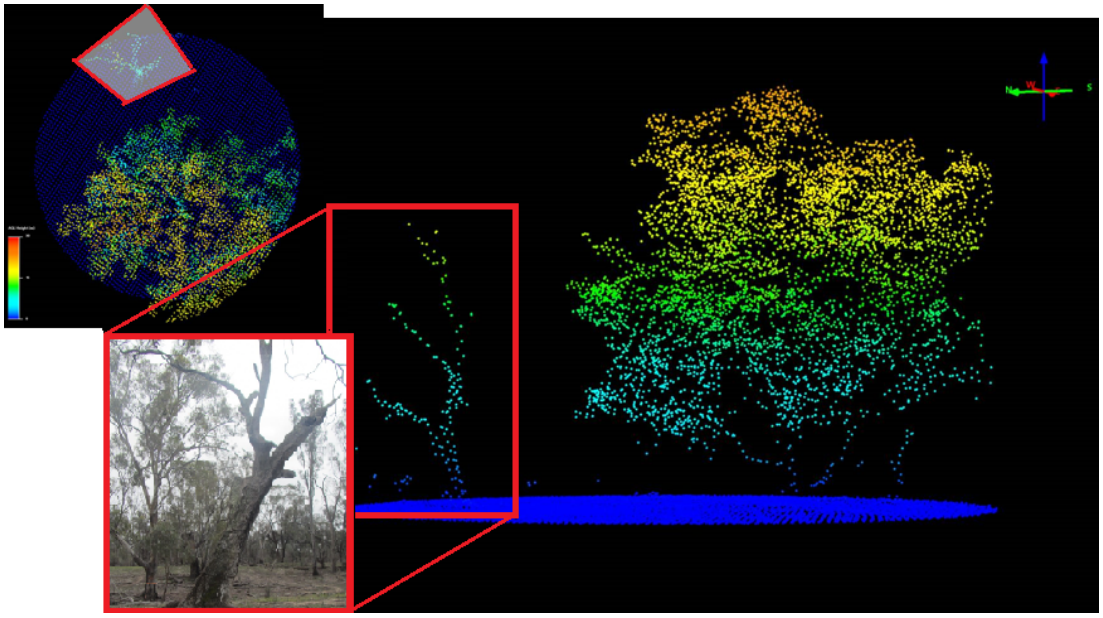

Figure 8-6: Example of a dead tree in relation to the discrete LiDAR point cloud.

by the magnetic bearing from the centroid of the plot in degrees (range $[1, 360]$) and the distance from the centroid in meters. The northing and easting coordinates of the geo-location of each tree were calculated in post-processing. Here it worth mentioning that a single tree may be recorded as multiple trees if there is a trunk split bellow the breast height of 1.3m. Furthermore, 91.59% are River Red Gum and the rest are Black Box (Eucalyptus largiflorens) and Wattle group (Acacia spp.).

Inside the field data, there are 260 dead trees recorded. Nevertheless, not all of those trees are considered useful for biodiversity. Dead trees with big Diameter at Breast Height (DBH) are more likely to contain hollows. Additionally, trees with DBH smaller than the footprint spacing of the LiDAR data are not identifiable from the FW LiDAR data. Table 8.1 shows the number of dead and alive trees in respect to their DBH.

Please note that the aforementioned field data were provided by Forestry Corporation of NSW, Wauchope, Australia and Interpine Ltd Group, New Zealand. For this thesis, a case study for collecting field data was conducted in New Forest, UK. This helped to better understand classification challenges in forestry applications. More information about this study is provided in Appendix B.

8.3 Methods and Algorithms / Statistical Analysis

steps

DBH	Dead Trees	Alive Trees
>2000	0	1
1000-2000	7	21
600-1000	8	146
400-600	26	290
300-400	32	286
200-300	50	462
100-200	125	904
<100	11	16
Total	260	2126

Table 8.1: Number of trees according to their DBH. **Note: I think it is in centimeter but I will confirm it with the company and add it afterwards.

- Subtract DTM From full-waveform LiDAR
- DASOS and 3D priors
- Random Forest for identifying the most significant features
- Nearest Neighbour
- Thinning Algorithm
- Remove Ground and noisy columns using Gaussian decomposition
- Evaluation

8.3.1 Subtract DTM from FW LiDAR

generating DTM beyond the scope of this research. The DTM is generated using the Quick Terrain Modeller from the discrete LiDAR using the parameters shown in Figure **??**.

DASOS has a feature for subtracting the DTM from the full-waveforms before generating the volumetric representation of the data. Figure **??** shows the DEM before and after the subtraction.

8.3.1.1 DASOS and 3D priors

The 3D shape signatures were generated by getting the distance distribution of random LiDAR point pairs of the two tree crown classes: Oaks and Douglas [64]

Here it is worth mentioning that this project is the first application of the new feature of DASOS that was released on the 20th of January 2017 [68].

In this chapter, the 3rd feature of DASOS (Table **??**) is used for generating 3D priors characterising dead standing Eucalypt trees. These 3D priors are used for detecting dead standing Eucalypt trees in native Australian forests.

like Viola but in 3D

the sets we create: 1. raw intensities

Figure 8-7

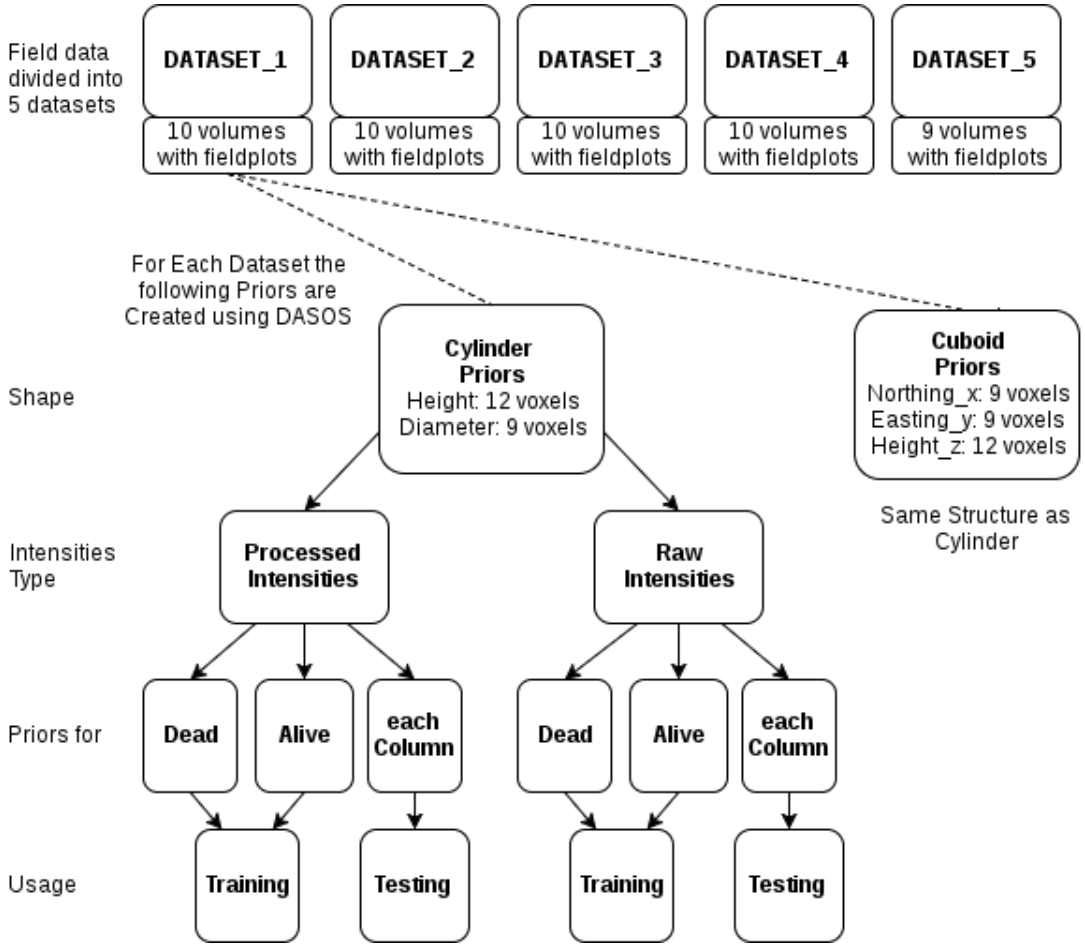

Figure 8-7: This figure shows what priors were created for testing and how they are divided for cross validation.

Explanation of the 3D priors Output with the Processed Intensities	
Label	**Description**
Height_Middle_Column	The height of the middle column of the prior
Height_Mean	The Mean height of all the columns included in the template
Height_Median	The Median height of all the columns included in the template
Height_Std	The Standard Deviation of the heights of the columns included in the template
Sum_Int_Diff_X	The Mirror Summed Difference of the intensities using the middle column in the x-axis as the axis of symmetry
Sum_Int_Diff_Y	The Mirror Summed Difference of the intensities using the middle column in the y-axis as the axis of symmetry
Sum_Int_Diff_Z	The Mirror Summed Difference of the intensities using the middle column in the z-axis as the axis of symmetry
Max_Int	The maximum intensity found inside the prior
Min_Int	The minimum intensity found inside the prior
Ave_Int	The average intensity of the voxels that contain an intensity above the isolevel
Median_Int	The median intensity of the voxels
Per_Int_Above_Iso	Percentage of voxels that contain an intensity above the isolevel
Dis_Mean	Mean distance from the central voxel to every voxel that contain san intensity above the isolevel
Dis_Median	Median distance from the central voxel to every voxel that contains an intensity above the isolevel
Dis_Std	The Standard Deviation of the distances between the central voxel and every voxel that contains an intensity above the isolevel
Top_Patch_Len_Middle_Col	The length of the top patch of the middle column of the prior

Top_Patch_Len_Mean	The Mean length of all the top patches
Top_Patch_Len_Median	The Median length of all the top patches
Top_Patch_Len_Std	The Standard Deviation of all the top patches
Mirror_Diff_X_Mean	The Mean Mirror Difference of the voxel intensities with the middle column of the x-axis as the symmetric axis
Mirror_Diff_X_Median	The Median Mirror Difference of the voxel intensities with the middle column of the x-axis as the symmetric axis
Mirror_Diff_X_Std	The Standard Deviation Mirror Difference of the voxel intensities with the middle column of the x-axis as the symmetric axis
Mirror_Diff_Y_Mean	The Mean Mirror Difference of the voxel intensities with the middle column of the y-axis as the symmetric axis
Mirror_Diff_Y_Median	The Median Mirror Difference of the voxel intensities with the middle column of the y-axis as the symmetric axis
Mirror_Diff_Y_Std	The Standard Deviation Mirror Difference of the voxel intensities with the middle column of the y-axis as the symmetric axis
Mirror_Diff_Z_Mean	The Mean Mirror Difference of the voxel intensities with the middle column of the z-axis as the symmetric axis
Mirror_Diff_Z_Median	The Median Mirror Difference of the voxel intensities with the middle column of the z-axis as the symmetric axis
Mirror_Diff_Z_Std	The Standard Deviation of the Mirror Difference of the voxel intensities with the middle column of the z-axis as the symmetric axis

Table 8.2: The three functionalities of DASOS

In the following section, the images and examples are taken from the Cylinder processed parameters but it done for all four test cases and cross validated using the 5 datasets division.

8.3.2 Random Forest

Images and examples for Cylinder processed parameters but it done for all four test cases and cross validated using the 5 datasets division.

Random Forest failed to find relation between the 3D priors with the Raw Intensities due to the irregular shapes of Eucalyptus trees and probably due to the scan from different angles. Raw Intensities may be useful for identifying pine trees in commercial forest, where the variance between each other is smaller.

Therefore from here we only test processed intensities with 3D cylindrical and 3D rectangular cuboid priors.

Identified the most significant features for detecting dead trees and then we build the following probabilistic model.

8.3.3 Probabilistic Model

We don't go straight to classification because in the testing data, we put a prior for each column and therefore many columns that contain dead trees are not marked correctly. And we wrote a probabilistic model using the most significant features identified by the random forest.

k-nearest neighbour: distance from the centre of mean for each of the first 5 significant features

from that get grey scale field of the results

8.3.4 Filtering and Local Maxima

Salt and pepper filter

Smoothing filter

Once the probability field is created, we smooth the image and detect the local maxima.

8.3.5 Ground Mask

Great histogram of the height map generated using the 2D metrics of DASOS.

Create three classes : ground, trees and noise

Because the DTM has been subtracted (Section 8.3.1), the ground is easily separated from the trees.

Mask out ground and noise

8.3.6 Threshold

if a local maxima is found but the probability of being a dead is low then it is not a dead tree. This is defined by a user defined constant threshold.

8.4 Results

8.5 Discussion

Chapter 9

Overall Results

Chapter 10

Conclusions

10.1 Contributions

Bibliography

[1] R. B. Smith, *Introduction to Hyperspectral Imaging.* MicroImages, 2014.

[2] W. Wanger, A. Ullrich, T. Melzer, C. Briese, and K. Kraus, "From single-pulse to ful-waveform airborne laser scanners," *ISPRS Journal of Photogrammetry and Remote Sensing*, vol. 60, pp. 100–112, 2004.

[3] A. Wehr and U. Lohr, "Airborne laser scanning - an introduction and overview," *ISPRS Journal of Photogrammerty and Remote Sensing*, vol. 54, pp. 68–82, 1999.

[4] C. Mallet and F. Bretar, "Full-waveform topographic lidar: State-of-the-art," *ISPRS Journal of Photogrametry and Remote Sensing*, vol. 64, pp. 1–16, 2009.

[5] K. Anderson, S. Hancock, M. Disney, and K. Gaston, "Is waveform worth it? a comparison of lidar approaches for vegetation and landscape characterization," *Remote Sensing in Ecology and Conservation*, 2015.

[6] A. Chauve, C. Mallet, F. Bretar, S. Durrieu, M. Deseilligny, and W. Puech, "Processing full-waveform lidar data: Modelling raw signals," *International Archives of Photogrammetry, Remote Sensing and Spatial Information Sciences*, 2007.

[7] *LAS Specification version 1.3-R1.* Bethesda, Maryland: American Society for Photogrammetry and Remote Sensing, 2010.

[8] M. Warren, *Full Waveform Upgrade.* NERC ARSF wiki, 2012.

[9] M. J. Sumnall, R. A. Hill, and S. A. Hinsley, "Comparison of small-footprint discrete return and full waveform airborne lidar data for estimating multiple forest variables," *Remote Sensing of Environment*, vol. 173, pp. 214–223, 2016.

[10] K. H. R. A. . Z. A. Lehner, H., "Consideration of laser pulse fluctuations and automatic gain control in radiometric calibration of airborne laser scanning data.," *Proceedings of 6th ISPRS Student Consortium and WG VI/5 Summer School*, 2011.

[11] I. Korpela, H. O. Ørka, H. V. Hyyppä, J., and T. Tokola, "Range and agc normalization in airborne discrete-return lidar intensity data for forest canopies," vol. 65, no. 4, pp. 369–379, 2010.

[12] M. Isenburg, *LAStools - efficient tools for LiDAR processing.* rapidlasso.

[13] M. Warren, B. Taylor, M. Grant, and J. D. Shutler, "Data processing of remorely sensed airborne hyperspectral data using the airborne processing library (apl)," *ScienceDirect, Computers and Geosciences*, vol. 64, 2014.

[14] W. Wanger, A. Ullrich, V. Ducic, T. Maizer, and N. Studnicka, "Gaussian decompositions and calibration of a novel small-footprint full-waveform digitising airborne laser scanner," *ISPRS Journal of Photogrammetry and Remote Sensing*, vol. 60, pp. 100–112, 2006.

[15] A. Neuenschwander, L. Magruder, and M. Tyler, "Landcover classification of small-footprint full-waveform lidar data," *Jounal of Applied Remote Sensing*, vol. 3, no. 1, pp. 033544–033544.

[16] J. Reitberger, P. Krzystek, and U. Stilla, "Analysis of full waveform LiDAR data for tree species classification," *International Journal of Remote Sensing*, vol. 29, no. 5, pp. 1407–1431, 2008.

[17] M. Isenburg, "Pulsewaves: An open, vendor-neutral, stand-alone, las-compatible full waveform lidar standard.," 2012.

[18] A. Chauve, F. Bretar, S. Durrieu, M. Pierrot-Deseilligny, and W. Puech, "Fullanalyze: A research tool for handling, processing and analysing full-waveform lidar data," *IEEE International Geoscience and Remote Sensing Symposium*, 2009.

[19] P. Bunting, J. Armston, D. Clewley, and R. M. Lucas, "Sorted pulse data (spd) library—part ii: A processing framework for lidar data from pulsed laser systems in terrestrial environments," *Computers & Geosciences*, vol. 56, pp. 207–215, 2013.

[20] A. Persson, U. Soderman, J. Topel, and S. Ahlberg, *Visualisation and Analysis of full-waveform airborne laser scanner data.* V/3 Workshop, Laser scanning 2005, 2005.

[21] L. Cao, N. Coops, L. Innes, J. Dai, and H. Ruan, "Tree species classification in subtropical forests using small-footprint full-waveform lidar data," *International Journal of Applied Earth Observation and Geoinformation*, vol. 49, pp. 39–51, 2016.

[22] S. Hancock, K. Anderson, M. Disney, and K. J. Gaston, "Measurement of fine-spatial-resolution 3d vegetation structure with airborne waveform lidar: Calibration and validation with voxelised terrestrial lidar.," *Remote Sensing of Environment*, vol. 188, pp. 37–50, 2017.

[23] M. Miltiadou, M. Grant, M. Brown, M. Warren, and E. Carolan, "Reconstruction of a 3d polygon representation from full-wavefrom lidar data," *RSPSoc Annual Conference 2014, New Sensors for a Changing World*, 2014.

[24] M. Miltiadou, M. A. Warren, M. Grant, and M. Brown, "Alignment of hyperspectral imagery and full-waveform lidar data for visualisation and classification purposes," *The International Archives of Photogrammetry, Remote Sensing and Spatial Information Sciences*, vol. 40, no. 7, p. 1257, 2015.

[25] R. Crippen, "Calculating the vegetation index faster," *Remote Sensing of Environment*, vol. 34, no. 1, pp. 71–73, 1990.

[26] R. N. Clark, G. A. Swayze, R. Wise, K. E. Livo, T. Hoefen, R. F. Kokaly, and S. J. Sutley, "Usgs digital spectral library splib06a," *US Geological Survey, Digital Data Series*, vol. 231, 2007.

[27] P. Hanrahan, "Ray tracing algebraic surfaces," *ACM SIGGRAPH Computer Graphics*, vol. 17, no. 3., 1983.

[28] H. Pfister, J. Hardenbergh, J. Knittel, H. Lauer, and L. Seiler, "The volumepro real-time ray-casting system," *Proceedings of the 26th annual conference on Computer graphics and interactive techniques*, pp. 251–260, 1999.

[29] J. Nickolls, I. Buck, M. Garland, and K. Skadron, "Scalable parallel programming with cuda," *Queue*, vol. 6, no. 2, pp. 40–55, 2008.

[30] C. Crassin, F. Neyret, S. Lefebvre, and E. Eisemann, "Gigavoxels: Ray-guided streaming for efficient and detailed voxel rendering," *Proceedings of the 2009 symosium on Interactive 3D graphics and games*, pp. 15–22, 2009.

[31] J. F. Blinn, *A Generalization of Algebraic Surface Drawing*, vol. 1. ACM Transactions on Graphics (TOG).

[32] A. Pasko and V. Savchenko, *Blending operations for the functionally based constructive geometry.* 1994.

[33] W. E. Lorensen and H. E. Cline, "Marching cubes: A high resolution 3d surface construction algorithm," *ACM Siggraph Computer Graphics*, vol. 21, pp. 163–169, 1987.

[34] M. L. Clark, D. A. Roberts, J. J. Ewel, and D. B. Clark, "Estimation of tropical rain forest aboveground biomas with small-foorprint lidar and hyperspectral sensors," *ScienceDirect, Remote Sensing of Enviroment*, vol. 115.

[35] J. E. Anderson, L. C. Plourde, M. E. Martin, B. H. Braswell, M. L. Smith, R. O. Dubayah, M. A. H. Dubayah, and J. B. Blair, "Integrating waveform lidar with hyperspectral imagery for inventory of a northern temperate forest," *Remote Sensing of Environment*, vol. 112, no. 4, pp. 1856–1870, 2008.

[36] H. Buddenbaum, S. Seeling, and J. Hill, "Fusion of full-waveform lidar and imaging spectroscopy remote sensing data for the characterization of forest stands," *International Journal of Remote Sensing*, vol. 32, no. 13, pp. 4511–4524, 2013.

[37] J. Heinzel and B. Koch, "Investigating multiple data sources for tree species classification in temperate forest and use for single tree delineation," *International Journal of Applied Earth Observation and Geoinformation*, vol. 18, pp. 101–110, 2012.

[38] R. G. Congalton, "A review of assessing the accuracy of classifications of remotely sensed data," *Remote Sensing of Enviroment*, vol. 37, no. 1.

[39] J. F. Franklin, H. H. Shugart, and M. E. Harmon, "Tree death as an ecological process," *BioScience*, vol. 17, no. 8, pp. 550–556, 1987.

[40] J. Siitonen, "Forest management, coarse woody debris and saproxylic organisms: Fennoscandian boreal forests as an example," *Ecological bulletins*, pp. 11–41, 2001.

[41] I. Hanski, "Extinction debt and species credit in boreal forests: modelling the consequences of different approaches to biodiversity conservation," *Annales Zoologici Fennici*, pp. 271–280, 2000.

[42] G. Peterson, C. R. Allen, and C. S. Holling, "Ecological resilience, biodiversity, and scale.," *Ecosystems*, vol. 1, no. 1, pp. 6–18, 1998.

[43] N. Abrego and I. Salcedo, "How does fungal diversity change based on woody debris type? a case study in northern spain," *Ekologija*, vol. 57, no. 3, 2011.

[44] J. N. Stokland and K. H. Larsson, "Legacies from natural forest dynamics: Different effects of forest management on wood-inhabiting fungi in pine and spruce forests," *Forest Ecology and Management*, vol. 261, no. 11, pp. 1707–1721, 2011.

[45] D. Lonsdale, M. Pautasso, and O. Holdenrieder, "Wood-decaying fungi in the forest: conservation needs and management options," *European Journal of Forest Research*, vol. 127, no. 1, pp. 1–22, 2008.

[46] P. Gibbons and D. Lindenmayer, *Tree Hollows and Wildlife Conservation in Australia*. CSIRO Publishing, 2002.

[47] D. B. Lindenmayer and J. T. Wood, "Long-term patterns in the decay, collapse, and abundance of trees with hollows in the mountain ash (eucalyptus regnans) forests of victoria, southeastern australia," *Canadian Journal of Forest Research*, vol. 40, no. 1, pp. 48–54, 2010.

[48] R. L. Goldingay, "Characteristics of tree hollows used by australian birds and bats," *Wildlife Research*, vol. 36, no. 5, pp. 394–409, 2009.

[49] "List of extinct, threatened and near threatened australian birds," *Environment Protection and Biodiversity Conservation Act*, 1999.

[50] Government of Western Australia, "Oarks and wildlife the list of threatened and priority fauna list," tech. rep., November 2015.

[51] Y. Kim, Z. Yang, W. B. Cohen, D. Pflugmacher, C. L. Lauver, and J. L. Vankat, "Distinguishing between live and dead standing tree biomass on the north rim of grand canyon national park, usa using small-footprint lidar data.," *Remote Sensing of Environment*, vol. 113, no. 11, pp. 2499–2510, 2009.

[52] P. Polewski, W. Yao, M. Heurich, P. Krzystek, and U. Stilla, "Detection of fallen trees in als point clouds using a normalized cut approach trained by simulation," *ISPRS Journal of Photogrammetry and Remote Sensing*, vol. 105, pp. 252–271, 2015.

[53] W. Mücke, B. Deák, H. M. Schroiff, A., and N. Pfeifer, "Detection of fallen trees in forested areas using small footprint airborne laser scanning data," *Canadian Journal of Remote Sensing*, vol. 139, no. s1, pp. S32–S40, 2013.

[54] W. Yao, P. Krzystek, and M. Heurich, "Identifying standing dead trees in forest areas based on 3d single tree detection from full-waveform lidar data," *ISPRS Annals of the Photogrammetry, Remote Sensing and Spatial Information Sciences*, vol. I-7, pp. 359–364, 2012.

[55] J. Pasher and D. J. King, "Mapping dead wood distribution in a temperate hardwood forest using high resolution airborne imagery," *Forest Ecology and Management*, vol. 258, no. 7, pp. 1536–1548, 2009.

[56] I. Shendryk, M. Broich, M. G. Tulbure, A. McGrath, D. Keith, and S. V. Alexandrov, "Mapping individual tree health using full-waveform airborne laser scans and imaging spectroscopy: A case study for a floodplain eucalypt forest," *Remote Sensing of Environment*, vol. 187, pp. 202–217, 2016.

[57] S. C. Popescu, R. H. Wynne, and R. F. Nelson, "Measuring individual tree crown diameter with lidar and assessing its influence on estimating forest volume and biomass," *Canadian journal of remote sensing*, vol. 29, no. 5, pp. 564–577, 2003.

[58] L. Jing, B. Hu, J. Li, and T. Noland, "Automated delineation of individual tree crowns from lidar data by multi-scale analysis and segmentation," *Photogrammetric Engineering & Remote Sensing*, vol. 78, no. 12, pp. 1275–1284, 2012.

[59] B. Hu, J. Li, L. Jing, and A. Judah, "Improving the efficiency and accuracy of individual tree crown delineation from high-density lidar data," *International Journal of Applied Earth Observation and Geoinformation*, vol. 26, pp. 145–15, 2014.

[60] S. C. Popescu and K. Zhao, "A voxel-based lidar method for estimating crown base height for deciduous and pine trees," *Remote sensing of environment*, vol. 112, no. 3, pp. 767–781, 2008.

[61] I. Shendryk, M. Broich, M. G. Tulbure, and S. V. Alexandrov, "Bottom-up delineation of individual trees from full-waveform airborne laser scans in a structurally complex eucalypt forest," *Remote Sensing of Environment*, vol. 173, pp. 69–83, 2016.

[62] J. L. Lovell, D. L. B. Jupp, G. J. Newnham, N. C. Coops, and D. S. Culvenor, "Simulation study for finding optimal lidar acquisition parameters for forest height retrieval.," *Forest Ecology and Management*, vol. 214, no. 1.

[63] P. Viola and M. Jones, "Rapid object detection using a boosted cascade of simple features," *Computer Vision and Pattern Recognition*, vol. 1, 2001.

[64] P. Dong, "Characterization of individual tree crowns using three-dimensional space signatures derived from lidar data.," *International Journal of Remote Sensing*, vol. 30, no. 24, pp. 6621–6628, 2009.

[65] J. Kerle, "Collation and review of stem density data and thinning prescriptions for the vegetation communities of new south wales," 2005.

[66] N. Wilson and N. C. C. of N.S.W, "The flooded gum trees : land use and management of river red gums in new south wales," *The Council, Sydney*, 1995.

[67] E. van Rees, "Trimble's ax60i and ax80," *GeoInformatics*, vol. 7, no. 5.

[68] M. Miltiadou, N. D. F. Campbell, M. Brown, A. S. G., M. Warren, D. Clewley, and M. Grant, "User guide of the 2nd version o dasos," 2017.

Appendix A

DASOS user guide

Appendix B

Case Study: Field Work in New Forest